AIMS Mathematics

AIMS Mathematics, 11(7): 21674–21703.
DOI: 10.3934/math.2026877
Received: 12 March 2026
Revised: 11 June 2026
Accepted: 29 June 2026
Published: 21 July 2026

https://www.aimspress.com/journal/Math

Research article

A hybrid LBKM/Semi-analytical approach for SH-Wave scattering in an elastic half-space

Shuwei Zhang[1], Shuihuai Yang[1], Xing Wei[2], Haowen Wu[1] and Linlin Sun[1,*]

[1] School of mathematics and statistics, Nantong University, Nantong, Jiangsu 226019, China
[2] School of Civil Engineering & Architecture, East China Jiaotong University, Nanchang 330013, China

* **Correspondence:** Email: rudong9110@163.com; Tel: +86051355003300.

Abstract: In this paper, a novel method combining the localized boundary knot method (LBKM) and a semi-analytical formulation is developed for analyzing SH wave scattering problems in half spaces. To solve the problem effectively, the computational domain is divided into a finite interior domain containing all scatterers and an infinite exterior region by a semicircle. In the finite domain, the LBKM, which is accurate and yields a sparse coefficient matrix, is employed. For the infinite exterior region, the solution is expressed by a semi-analytical formulation that exactly satisfies both the governing equation and the Sommerfeld radiation condition. The two formulations are then coupled through interface conditions. Three numerical examples involving the scattering of SH waves by canyons, underground tunnels, and inclusions were conducted to validate the proposed method. Its superior performance is illustrated through a comparison with the generalized finite difference method, localized method of fundamental solution, and radial point interpolation method. For the cases without analytical solutions, the effectiveness of the proposed approach is validated via the results from the finite element method.

Keywords: localized boundary knot method; Meshless method; SH wave; semi-analytical formulation; half spaces
Mathematics Subject Classification: 65N85, 74J20

1. Introduction

Earthquakes often cause severe damage on the ground surface. The presence of both natural and artificial underground structures, such as canyons, inclusions, and tunnels, can further influence ground deformation characteristics during seismic wave propagation. Numerous studies have been conducted to investigate the scattering behavior of SH waves, a type of seismic wave, around these features. Among various approaches, deriving analytical solutions is widely regarded as the most accurate method. Todorovska and Lee [1] obtained an analytical solution for the scattering of SH waves by a shallow circular alluvial valley based on the Bessel-Fourier series expansion. Smerzini et al. [2] developed corresponding analytical solutions for cylindrical underground structures (e.g., cavities and inclusions) under SH-wave excitation and further analyzed the influence of such structures on ground motion responses. Zhang et al. [3] derived an analytical solution for the interaction of a surficial alluvial valley and an embedded underground tunnel subjected to plane SH waves. Although a considerable number of analytical solutions for SH-wave scattering problems have been reported in the literature, the scatterers considered in these studies are mostly regular in geometry. For problems involving irregular scatterers, numerical methods are generally more applicable.

Up to now, numerous numerical methods have been employed to solve various wave propagation problems, such as the finite element method (FEM) [4–6], the boundary element method (BEM) [7–9], physics-informed neural networks (PINNs) [10,11], and meshless methods [12–14]. The FEM is employed to analyze the scattering of SH waves from a non-circular cavity embedded in strip media by Xiang et al. [15]. Ge [16] and Mojtabazadeh-Hasanlouei et al. [17] applied the BEM to solve the scattering problems of transient and time-harmonic SH waves in a half space, respectively. In [18], the PINNs are applied to the parameter inversion of seismic waves. Shaker et al. [19] employed the meshless local Petrov–Galerkin (MLPG) method combined with a perfectly matched layer (PML) to simulate wave propagation in a poroelastic half space. In [20], the generalized finite difference method (GFDM) with PML is applied to solve SH wave scattering problem. Using the modified meshfree radial point interpolation method (RPIM), Xue et al. [21] solved transient wave propagation problems. Shi et al. [22] implemented the local radial basis function method (LRBF) to analyze elastic wave problems. Liu et al. [23] integrated the fast multipole method (FMM) with the method of fundamental solutions (MFS) to analyze SH-wave scattering problems at different frequencies. It is noteworthy that the MFS, as a meshless method, requires simpler pre-processing compared to mesh-based methods like the FEM. Unlike the BEM, it avoids the need to handle singular and nearly singular integrals. Furthermore, when compared to the PINNs, the MFS demonstrates superior computational efficiency. Additionally, because its basis functions satisfy the governing equations, the MFS belongs to the category of semi-analytical methods [24–26], and consequently its accuracy and efficiency surpass those of the other meshless methods mentioned above. It is an effective numerical method for solving wave propagation problems.

In the MFS, fundamental solutions (FSs) serve as the kernel functions, and source points must be placed on the artificial boundary outside the physical domain to circumvent the singularity inherent in the FSs. Although there exist several methods for determining the optimal location of source points [27], they may suffer from low computational efficiency and are not necessarily effective for all engineering problems. To overcome the limitations of the MFS, the boundary knot method (BKM) [28] was proposed in 2002. The method uses the non-singular general solution that satisfies the governing equations, instead of the FS, thereby eliminating the need for artificial boundaries in the MFS. The BKM inherits the advantages of the MFS, including high computational accuracy and rapid convergence. It has been successfully applied to solve various wave propagation problems [29–31]. However, a limitation of the BKM is that it produces a dense and ill-conditioned coefficient matrix. Recently, a localized boundary knot method (LBKM) [32] is proposed. The method divides the entire computational domain into overlapping subdomains and constructs a system of linear equations based on each subdomain. Consequently, the resulting coefficient matrix is sparse and exhibits significantly better properties than that generated by the traditional BKM [33], thereby effectively overcoming the drawbacks of the BKM. Furthermore, the non-singular general solution is used for interpolation on local subdomains, which leads to the high computational accuracy of the LBKM. The LBKM has been successfully used to solve acoustic [34] and convection–diffusion [35] problems.

In this paper, the LBKM is applied to SH wave scattering problems. Since the LBKM requires the distribution of nodes throughout the entire domain, it cannot be directly applied to solve the considered problem. To address this, the domain is divided into a finite domain and a semi-infinite region. The LBKM is employed to compute the variables within the finite domain, while those in the semi-infinite region are approximated using a semi-analytical formulation. Section 2 of the paper presents the basic equations for the SH-wave scattering problem. Section 3 describes the LBKM and semi-analytical formulations. Section 4 provides three numerical examples to demonstrate the validity of the proposed method. The final section summarizes the conclusions.

2. Problem description

The scattering problem of plane harmonic SH waves is considered in a semi-infinite isotropic elastic medium containing valleys, cavities, and inclusions, as shown in Figure 1. Omitting the time factor $e^{j\omega t}$, the governing equation for the considered problem is:

$$\mu\nabla^2 u + \rho\omega^2 u = 0, \boldsymbol{x} \in \Omega, \tag{1}$$

where μ is shear modulus; ρ denotes density; ω represents angular frequency; $\nabla = (\partial/\partial x_1, \partial/\partial x_2)^{\mathrm{T}}$ stands for gradient operator, $\mathrm{j} = \sqrt{-1}$; and u is displacement field, which is composed of the scattered wave u_{sc} and free field u_{ff}. The free field comprises the incident wave (u_{inc}) and the reflected wave (u_{ref}) fields, expressed as:

$$u_{ff} = u_{inc} + u_{ref}. \tag{2}$$

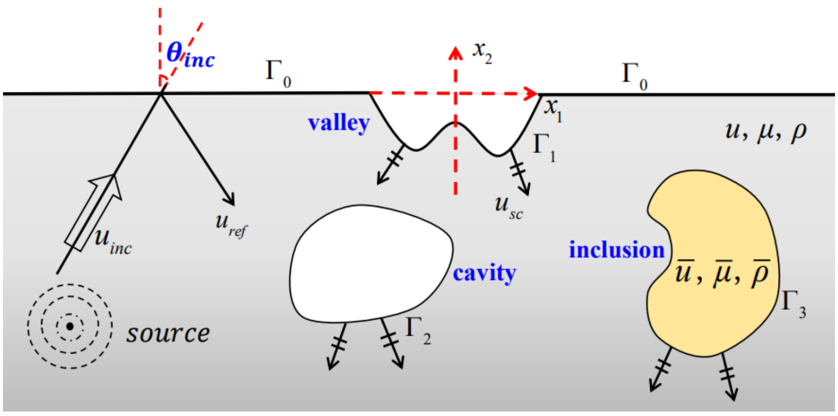

Figure 1. Problem description.

When the incident angle is θ_{inc}, the expression for the incident wave is

$$u_{inc} = e^{-j\lambda\left(x_1\cos(\theta_{inc})+x_2\sin(\theta_{inc})\right)}, \tag{3}$$

in which $\lambda = \omega/c$, $c = \sqrt{\mu/\rho}$. The reflected wave is

$$u_{ref} = e^{-j\lambda\left(x_1\cos(\theta_{inc}) - x_2\sin(\theta_{inc})\right)}. \tag{4}$$

To ensure the uniqueness of the solution, the following boundary conditions are imposed on the boundary:

$$t_3 = \mu\frac{\partial u}{\partial \boldsymbol{n}} = \mu\frac{\partial u}{\partial x_1}n_1 + \mu\frac{\partial u}{\partial x_2}n_2 = 0\text{Pa}, \boldsymbol{x} \in \Gamma_0 \cup \Gamma_1 \cup \Gamma_2, \tag{5}$$

that is,

$$\mu\frac{\partial u_{sc}}{\partial x_1}n_1 + \mu\frac{\partial u_{sc}}{\partial x_2}n_2 = -\mu\frac{\partial u_{ff}}{\partial x_1}n_1 - \mu\frac{\partial u_{ff}}{\partial x_2}n_2, \tag{6}$$

with $(n_1,n_2)^{\mathrm{T}}$ the unit normal vector. At infinity, the scattered wave field satisfies the following Sommerfeld radiation condition:

$$\lim_{r\to\infty} r^{\frac{1}{2}}\left(\frac{\partial u_{sc}}{\partial r} + j\lambda u_{sc}\right) = 0. \tag{7}$$

For the case involving inclusions, the following interface continuity conditions are prescribed:

$$\begin{cases} u = \bar{u} \\ \mu\dfrac{\partial u}{\partial \boldsymbol{n}} = \bar{\mu}\dfrac{\partial \bar{u}}{\partial \boldsymbol{n}} \end{cases}, \boldsymbol{x} \in \Gamma_3, \tag{8}$$

where $\bar{\mu}$ and $\bar{u}$ are the shear modulus and displacement field inside the inclusion, respectively.

Due to the fact that the free field is known, the LBKM is used to solve the scattering field u_{sc} and the variable $\bar{u}$ in the inclusion.

3. Methodology

The LBKM requires discretization of the entire computational domain. However, this is infeasible due to the domain's infinite extent. As shown in Figure 2, this paper uses a semicircle with a radius of R_I to partition the computational domain into a finite domain and a regular infinite domain, where the finite domain contains all the scatterers (i.e., canyons, cavities, and inclusions). To make the problem well-posed, the following additional continuity condition must be imposed on the interface Γ_I:

$$\begin{cases} u_{sc}^{(i)} = u_{sc}^{(e)} \\ \dfrac{\partial u_{sc}^{(i)}}{\partial \boldsymbol{n}^{(i)}} = -\dfrac{\partial u_{sc}^{(e)}}{\partial \boldsymbol{n}^{(e)}} \end{cases}, \tag{9}$$

where $u_{sc}^{(i)}$ and $u_{sc}^{(e)}$ are the scattering fields in finite and infinite domains, respectively. The vectors $\boldsymbol{n}^{(i)}$ and $\boldsymbol{n}^{(e)}$ denote the outward unit normal vectors of the interior and exterior domains at Γ_I, respectively. In this paper, variables within the finite domain are solved using the LBKM, while those in the infinite domain are approximated by semi-analytical formulations.

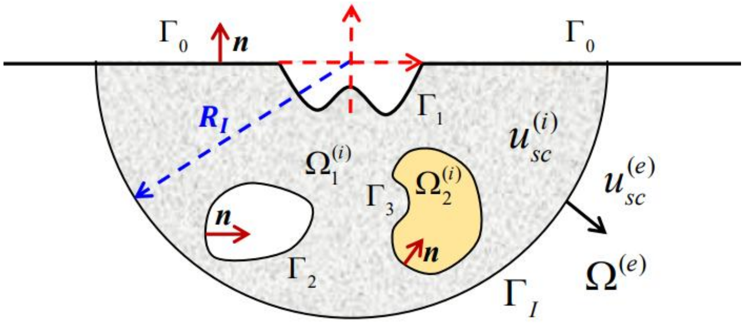

Figure 2. Schematic diagram of dividing the computational domain into a finite domain and a regular infinite domain.

3.1. Localized boundary knot method

During the implementation of the LBKM, the finite domain and boundary in Figure 2 are first discretized into discrete nodes. Specifically, the nodes $\{\hat{\boldsymbol{y}}_j\}_{j=1}^{N_1^{(i)}}$ are distributed within domain $\Omega_1^{(i)}$, $\{\hat{\boldsymbol{y}}_j\}_{j=1+N_1^{(i)}}^{N_b+N_1^{(i)}}$ on boundary $\Gamma_0\cup\Gamma_1\cup\Gamma_2$, $\{\bar{\boldsymbol{y}}_j\}_{j=1}^{N_I}$ on Γ_I, $\{\tilde{\boldsymbol{y}}_j\}_{j=1}^{N_3}$ on Γ_3, and $\{\hat{\boldsymbol{y}}_j\}_{j=1}^{N_2^{(i)}}$ within $\Omega_2^{(i)}$. To facilitate reader comprehension, the derivation process of the LBKM formulation is introduced based on the nodes from the domain $\Omega_1^{(i)}$ and its boundary. For an arbitrary node $\boldsymbol{y}_k\in\boldsymbol{D}=\{\hat{\boldsymbol{y}}_j\}_{j=1}^{N_b+N_1^{(1)}}\cup\{\bar{\boldsymbol{y}}_j\}_{j=1}^{N_I}\cup\{\tilde{\boldsymbol{y}}_j\}_{j=1}^{N_3}$, which is usually defined as the central node, its m nearest neighboring nodes are selected to form a local influence domain $\boldsymbol{\Xi}_k=\{\boldsymbol{y}_k^{(0)},\boldsymbol{y}_k^{(1)},\ldots,\boldsymbol{y}_k^{(m)}\}\subset\boldsymbol{D}$ ($\boldsymbol{y}_k^{(0)}=\boldsymbol{y}_k$), where each $\boldsymbol{y}_k^{(j)}(j>0)$ is termed a supporting node, as shown in Figure 3.

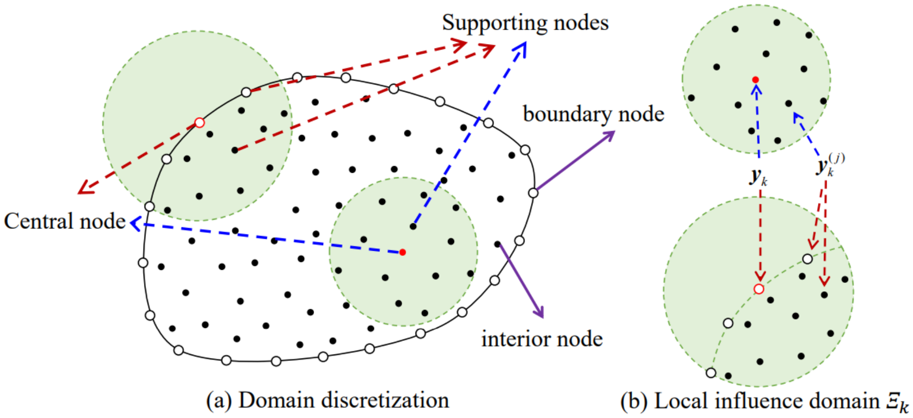

Figure 3. Schematic diagrams of (a) domain discretization and (b) local influence domain (green region) for boundary and interior nodes.

The variable at the node in Ξ_k can be approximated by

$$u_{sc}^{(i)}(\boldsymbol{y}_k^{(j)})=\sum_{n=1}^{m}\beta_k^{(n)}J_0\left(\lambda\left\|\boldsymbol{y}_k^{(j)}-\boldsymbol{y}_k^{(n)}\right\|_2\right)=\boldsymbol{G}_k^{(j)}\boldsymbol{\beta}^{(k)},\ j=1,2,\ldots,m, \tag{10}$$

where $\beta_k^{(n)}$ is the unknown coefficient, J_0 denotes zeroth-order Bessel function of the first kind, $\boldsymbol{G}_k^{(j)}=\left[J_0\left(\lambda\left\|\boldsymbol{y}_k^{(j)}-\boldsymbol{y}_k^{(1)}\right\|_2\right),J_0\left(\lambda\left\|\boldsymbol{y}_k^{(j)}-\boldsymbol{y}_k^{(2)}\right\|_2\right),\ldots,J_0\left(\lambda\left\|\boldsymbol{y}_k^{(j)}-\boldsymbol{y}_k^{(m)}\right\|_2\right)\right]$ and $\boldsymbol{\beta}^{(k)}=\left[\beta_k^{(1)},\beta_k^{(2)},\ldots,\beta_k^{(m)}\right]^{\mathrm{T}}$.

Writing Eq (10) in matrix form yields

$$\boldsymbol{A}^{(k)}\boldsymbol{\beta}^{(k)}=\boldsymbol{b}^{(k)}, \tag{11}$$

with

$$\boldsymbol{A}^{(k)}=\begin{bmatrix} J_0\left(\lambda\left\|\boldsymbol{y}_k^{(1)}-\boldsymbol{y}_k^{(1)}\right\|_2\right) & J_0\left(\lambda\left\|\boldsymbol{y}_k^{(1)}-\boldsymbol{y}_k^{(2)}\right\|_2\right) & \cdots & J_0\left(\lambda\left\|\boldsymbol{y}_k^{(1)}-\boldsymbol{y}_k^{(m)}\right\|_2\right) \\ J_0\left(\lambda\left\|\boldsymbol{y}_k^{(2)}-\boldsymbol{y}_k^{(1)}\right\|_2\right) & J_0\left(\lambda\left\|\boldsymbol{y}_k^{(2)}-\boldsymbol{y}_k^{(2)}\right\|_2\right) & \cdots & J_0\left(\lambda\left\|\boldsymbol{y}_k^{(2)}-\boldsymbol{y}_k^{(m)}\right\|_2\right) \\ \vdots & \vdots & \ddots & \vdots \\ J_0\left(\lambda\left\|\boldsymbol{y}_k^{(m)}-\boldsymbol{y}_k^{(1)}\right\|_2\right) & J_0\left(\lambda\left\|\boldsymbol{y}_k^{(m)}-\boldsymbol{y}_k^{(2)}\right\|_2\right) & \cdots & J_0\left(\lambda\left\|\boldsymbol{y}_k^{(m)}-\boldsymbol{y}_k^{(m)}\right\|_2\right) \end{bmatrix},$$

and

$$\boldsymbol{b}^{(k)}=\left[u_{sc}^{(i)}(\boldsymbol{y}_k^{(1)}),u_{sc}^{(i)}(\boldsymbol{y}_k^{(2)}),\ldots,u_{sc}^{(i)}(\boldsymbol{y}_k^{(m)})\right]^{\mathrm{T}}.$$

Solving the linear equations (11) leads to

$$\boldsymbol{\beta}^{(k)}=\boldsymbol{H}^{(k)}\boldsymbol{b}^{(k)}, \tag{12}$$

where $\boldsymbol{H}^{(k)}$ is the inverse of $\boldsymbol{A}^{(k)}$, computed using the MATLAB command "pinv($\boldsymbol{A}^{(k)}$, *tol*)". Unless otherwise specified, *tol* is set to 10^{-10} in the following.

If $\boldsymbol{y}_k^{(0)}$ is an interior node, the scattering field at $\boldsymbol{y}_k^{(0)}$ can be expressed as

$$\begin{aligned} u_{sc}^{(i)}(\boldsymbol{y}_k^{(0)}) &= \sum_{n=1}^{m}\beta_k^{(n)}J_0\left(\lambda\left\|\boldsymbol{y}_k^{(0)}-\boldsymbol{y}_k^{(n)}\right\|_2\right) \\ &= \boldsymbol{G}_k^{(0)}\boldsymbol{\beta}^{(k)}=\boldsymbol{G}_k^{(0)}\boldsymbol{H}^{(k)}\boldsymbol{b}^{(k)}=\boldsymbol{w}_k\boldsymbol{b}^{(k)}=\sum_{n=1}^{m}w_k^{(n)}u_{sc}^{(i)}(\boldsymbol{y}_k^{(n)}), \end{aligned} \tag{13}$$

that is,

$$u_{sc}^{(i)}(\boldsymbol{y}_k^{(0)})-\sum_{n=1}^{m}w_k^{(n)}u_{sc}^{(i)}(\boldsymbol{y}_k^{(n)})=0, \tag{14}$$

with $\boldsymbol{w}_k=\boldsymbol{G}_k^{(0)}\boldsymbol{H}^{(k)}=[w_k^{(1)},w_k^{(2)},\ldots,w_k^{(m)}]$. Equation (14) is the linear equation for each interior node in $\Omega_1^{(i)}$.

If $\boldsymbol{y}_k^{(0)}$ is the boundary node, we have

$$\frac{\partial u_{sc}^{(i)}(\boldsymbol{y}_k^{(0)})}{\partial \boldsymbol{n}} = \sum_{n=1}^{m} \beta_k^{(n)} \frac{\partial J_0\left(\lambda \left\| \boldsymbol{y}_k^{(0)} - \boldsymbol{y}_k^{(n)} \right\|_2\right)}{\partial \boldsymbol{n}}$$
$$= \boldsymbol{N}_k^{(0)} \boldsymbol{\beta}^{(k)} = \boldsymbol{N}_k^{(0)} \boldsymbol{H}^{(k)} \boldsymbol{b}^{(k)} = \bar{\boldsymbol{w}}_k \boldsymbol{b}^{(k)} = \sum_{n=1}^{m} \bar{w}_k^{(n)} u_{sc}^{(i)}(\boldsymbol{y}_k^{(n)}). \tag{15}$$

The expressions of the symbols in the above formula are as follows:

$$\boldsymbol{N}_k^{(0)} = \left(\frac{\partial J_0\left(\lambda \left\| \boldsymbol{y}_k^{(0)} - \boldsymbol{y}_k^{(1)} \right\|_2\right)}{\partial \boldsymbol{n}}, \frac{\partial J_0\left(\lambda \left\| \boldsymbol{y}_k^{(0)} - \boldsymbol{y}_k^{(2)} \right\|_2\right)}{\partial \boldsymbol{n}}, \dots, \frac{\partial J_0\left(\lambda \left\| \boldsymbol{y}_k^{(0)} - \boldsymbol{y}_k^{(m)} \right\|_2\right)}{\partial \boldsymbol{n}} \right),$$

$$\bar{\boldsymbol{w}}_k = \boldsymbol{N}_k^{(0)} \boldsymbol{H}^{(k)} = \left(\bar{w}_k^{(1)}, \bar{w}_k^{(2)}, \dots, \bar{w}_k^{(m)} \right).$$

Substituting Eq (15) into the boundary condition (6), the linear equation for the node on boundary $\Gamma_0 \cup \Gamma_1 \cup \Gamma_2$ can be obtained:

$$\mu \sum_{n=1}^{m} \bar{w}_k^{(n)} u_{sc}^{(i)}(\boldsymbol{y}_k^{(n)}) = -\mu \frac{\partial u_{ff}(\boldsymbol{y}_k^{(0)})}{\partial \boldsymbol{n}}. \tag{16}$$

Next, the case of inclusions within the computational domain is considered. Assuming $\boldsymbol{z}_l^{(0)} \in \bar{\boldsymbol{D}} = \left\{ \tilde{\boldsymbol{y}}_j \right\}_{j=1}^{N_3} \cup \left\{ \hat{\boldsymbol{y}}_j \right\}_{j=1}^{N_2^{(i)}}$ is a node in the inclusion, the corresponding local influence domain is $\bar{\Xi}_l = \left\{ \boldsymbol{z}_l^{(0)}, \boldsymbol{z}_l^{(1)}, \dots, \boldsymbol{z}_l^{(m)} \right\} \subset \bar{\boldsymbol{D}}$. The approximate formula similar to Eq (10) is

$$\bar{u}(\boldsymbol{z}_l^{(j)}) = \sum_{n=1}^{m} \bar{\beta}_l^{(n)} J_0\left(\bar{\lambda} \left\| \boldsymbol{z}_l^{(j)} - \boldsymbol{z}_l^{(n)} \right\|_2 \right), j = 1, 2, \dots, m, \tag{17}$$

where $\bar{\beta}_l^{(n)}$ is the unknown coefficient, $\bar{\lambda} = \omega / \bar{c}$ with $\bar{c} = \sqrt{\bar{\mu} / \bar{\rho}}$. Using the same derivation as above yields the following equations:

$$\bar{u}(\boldsymbol{z}_l^{(0)}) = \sum_{n=1}^{m} \hat{w}_l^{(n)} \bar{u}(\boldsymbol{z}_l^{(n)}), \boldsymbol{z}_l^{(0)} \in \Omega_2^{(i)}, \tag{18}$$

$$\frac{\partial \bar{u}(\boldsymbol{z}_l^{(0)})}{\partial \boldsymbol{n}} = \sum_{n=1}^{m} \tilde{w}_l^{(n)} \bar{u}(\boldsymbol{z}_l^{(n)}), \boldsymbol{z}_l^{(0)} \in \Gamma_3. \tag{19}$$

The derivation of coefficients $\hat{w}_l^{(n)}$ and $\tilde{w}_l^{(n)}$ follows the same procedure as that for $w_k^{(n)}$ and $\bar{w}_k^{(n)}$ in Eqs (13) and (15).

When $\boldsymbol{y}_k^{(0)} = \boldsymbol{z}_l^{(0)} \in \Gamma_3$, with the aid of Eqs (15) and (19), the interface conditions (8) can be converted into the following linear equations

$$u_{sc}^{(i)}(\boldsymbol{y}_k^{(0)}) - \bar{u}(\boldsymbol{z}_l^{(0)}) = -u_{ff}(\boldsymbol{y}_k^{(0)}), \tag{20}$$

$$\mu \sum_{n=1}^{m} \bar{w}_k^{(n)} u_{sc}^{(i)}(\boldsymbol{y}_k^{(n)}) - \bar{\mu} \sum_{n=1}^{m} \tilde{w}_l^{(n)} \bar{u}(\boldsymbol{z}_l^{(n)}) = -\mu \frac{\partial u_{ff}(\boldsymbol{y}_k^{(0)})}{\partial \boldsymbol{n}}. \tag{21}$$

3.2. Semi-analytical formulation for the problem in semi-infinite domain

The LBKM can only be applied to approximate variables in finite domains. In this section, the scattering field in the infinite domain $\Omega^{(e)}$ (Figure 2) is represented using analytical formulations. Before giving the analytical formula, the boundary conditions on Γ_0 ($x_2 = 0$, i.e., $\theta = 0$ and $\theta = -\pi$) are first transformed into polar coordinates, yielding the following expression:

$$\mu\frac{\partial u_{sc}}{\partial \boldsymbol{n}} = \mu\left(-\frac{1}{r}\frac{\partial u_{sc}}{\partial \theta}\sin\theta + \frac{\partial u_{sc}}{\partial r}\cos\theta\right)n_1 + \mu\left(\frac{1}{r}\frac{\partial u_{sc}}{\partial \theta}\cos\theta + \frac{\partial u_{sc}}{\partial r}\sin\theta\right)n_2 = 0, \tag{22}$$

that is,

$$\frac{\partial u_{sc}}{\partial \theta} = 0. \tag{23}$$

Based on boundary condition (23), once the boundary condition on Γ_I is known, the analytical expression of the scattered field in $\Omega^{(e)}$ can be obtained by the method of separation of variables. To apply this method, the governing equation is first transformed into polar coordinates. Solving the resulting equation yields the following set of eigenfunction terms:

$$\begin{aligned}&\{K_0(\mathrm{j}\lambda r), K_1(\mathrm{j}\lambda r)\cos(\theta), K_2(\mathrm{j}\lambda r)\cos(2\theta), \ldots, K_n(\mathrm{j}\lambda r)\cos(n\theta), \ldots\\ &K_1(\mathrm{j}\lambda r)\sin(\theta), K_2(\mathrm{j}\lambda r)\sin(2\theta), \ldots, K_n(\mathrm{j}\lambda r)\sin(n\theta), \ldots\}.\end{aligned} \tag{24}$$

To successfully derive the analytical solution, the eigenfunction terms must satisfy boundary condition (23). In this case, the terms containing $\sin(n\theta)$ do not meet the requirement because their angular derivatives do not vanish at $\theta = 0$ and -π. The remaining terms that satisfy both the governing equation and boundary condition (23) are

$$\{K_0(\mathrm{j}\lambda r), K_1(\mathrm{j}\lambda r)\cos(\theta), K_2(\mathrm{j}\lambda r)\cos(2\theta), \ldots, K_n(\mathrm{j}\lambda r)\cos(n\theta), \ldots\}. \tag{25}$$

With the aid of the eigenfunction terms in Eq (25), the scattered field in domain $\Omega^{(e)}$ can be expressed as [36,37]

$$u_{sc}^{(e)} = \sum_{n=0}^{\infty}\alpha_n K_n(\mathrm{j}\lambda r)\cos(n\theta), r \ge R_I. \tag{26}$$

Assuming Dirichlet boundary conditions are prescribed on boundary Γ_I with a known boundary value g(θ), the expression for the unknown coefficients is

$$\alpha_n = \frac{\int_{-\pi}^{0} g(\theta)\cos(n\theta)d\theta}{K_n(\mathrm{j}\lambda R_I)}\gamma_n, \gamma_n = \begin{cases}1/\pi, n = 0\\ 2/\pi, n > 0\end{cases}. \tag{27}$$

Obviously, $\int_{-\pi}^{0} g(\theta)\cos(n\theta)d\theta = \left[\frac{1}{n^2}\left(g'(0) - (-1)^n g'(-\pi) - \int_{-\pi}^{0} g''(\theta)\cos(n\theta)d\theta\right)\right] \to 0$ as $n \to \infty$. Substituting Eq (27) into Eq (26) gives

$$u_{sc}^{(e)} = \sum_{n=0}^{\infty}\frac{K_n(\mathrm{j}\lambda r)}{K_n(\mathrm{j}\lambda R_I)}\gamma_n\cos(n\theta)\int_{-\pi}^{0} g(\theta)\cos(n\theta)d\theta. \tag{28}$$

Since $\left|\frac{K_n(\mathrm{j}\lambda r)}{K_n(\mathrm{j}\lambda R_I)}\right| \le 1$ when $r \ge R_I$, the term indexed by n in Eq (28) generally decays at a rate of O(1/n^2) or faster as n increases. Similarly, when Neumann boundary conditions are imposed on the boundary Γ_I, similar conclusions can be drawn. In practical, the boundary condition on Γ_I is unknown, so the analytic formula for α_n cannot be derived. Here, a numerical technique is used to estimate the unknown coefficients, and for the purpose of numerical implementation, the following approximate expression is adopted:

$$u_{sc}^{(e)} = \sum_{n=0}^{n_s} \bar{\alpha}_n \frac{K_n(\mathrm{j}\lambda r)}{K_n(\mathrm{j}\lambda R_I)} \cos(n\theta). \tag{29}$$

with $\bar{\alpha}_n = K_n(\mathrm{j}\lambda R_I)\alpha_n$. It is worth noting that Eq (29) is obtained by truncating Eq (26) and adjusting the coefficients, where the terms from n = 0 to n = n_s are retained, giving a total of n_s +1 terms. According to the analysis in the paragraph below Eq (28), this truncation is reasonable. In addition, the purpose of adjusting the coefficients is to prevent numerical instability in the subsequent construction of the numerical solution scheme, since $|K_n(\mathrm{j}\lambda r)|$ can become extremely large when n is large.

Substituting Eqs (15) and (29) into the continuity condition (9), the following linear equations can be obtained:

$$\begin{cases} u_{sc}^{(i)}(\boldsymbol{y}_k^{(0)}) = \sum_{n=0}^{n_s} \bar{\alpha}_n \frac{K_n(\mathrm{j}\lambda r_k)}{K_n(\mathrm{j}\lambda R_I)} \cos(n\theta_k) \\ \sum_{n=1}^{m} \bar{w}_k^{(n)} u_{sc}^{(i)}(\boldsymbol{y}_k^{(n)}) = \sum_{n=0}^{n_s} \frac{\bar{\alpha}_n}{K_n(\mathrm{j}\lambda R_I)} \frac{\partial K_n(\mathrm{j}\lambda r_k)}{\partial r} \cos(n\theta_k) \end{cases}, \boldsymbol{y}_k^{(0)} \in \Gamma_I, \tag{30}$$

with (r_k, θ_k) the polar coordinates corresponding to point $\boldsymbol{y}_k^{(0)}$.

Based on the derivations in Sections 3.1 and 3.2, the system of linear equations for the entire problem is composed of Eqs (14), (16), (18), (20), (21), and (30). There are a total of $2N_I + N_b + N_1^{(i)} + 2N_3 + N_2^{(i)}$ equations involving $N_I + N_b + N_1^{(i)} + 2N_3 + N_2^{(i)} + n_s + 1$ unknown coefficients. During implementation, $N_I \ge n_s + 1$ is maintained to guarantee solution uniqueness. After solving the linear equations, the variables at all nodes can be determined.

4. Example

This section examines the computational accuracy and feasibility of the proposed method through three numerical examples. Unless otherwise specified, the material properties are: μ = 20 GPa, ρ = 2650 kg/m^3. The formula for calculating the average relative error is

$$arerr(u) = \sqrt{\frac{\sum_{n=1}^{NT} \left(u(\boldsymbol{y}_n) - \hat{u}(\boldsymbol{y}_n)\right)^2}{\sum_{n=1}^{NT} u^2(\boldsymbol{y}_n)}}, \tag{31}$$

where $\hat{u}$ and u represent the numerical and analytical (or reference) displacement fields, respectively; $\boldsymbol{y}_n$ stands for the test point; and NT denotes the number of test points. For convenience of analysis, the dimensionless frequency is defined as $\eta = \omega a/(\pi c)$, with a as the geometric dimension of the computational domain.

4.1. Semicircular canyons

The first example examines the validity of the proposed method for SH wave scattering by semicircular canyons in a semi-infinite domain.

4.1.1. Single semi-circular canyon

As shown in Figure 4, the single-canyon case is considered first. The analytical solution [38] is

$$u(r,\theta) = u_{ff} + \sum_{k=0}^{\infty} \varepsilon_k H_k^{(2)}(\lambda r)\cos(k\theta), \tag{32}$$

where $\varepsilon_0 = -2\dfrac{J_1(\lambda a)}{H_1^{(2)}(\lambda a)}$ and $\varepsilon_k = -4(-\mathrm{j})^k \cos(k\theta_{inc})\dfrac{\lambda a J_{k-1}(\lambda a) - kJ_k(\lambda a)}{\lambda a H_{k-1}^{(2)}(\lambda a) - kH_k^{(2)}(\lambda a)}$ with J_k the Bessel function of the first kind of order k and $H_k^{(2)}$ the Hankel function of the second kind of order k. When applying the proposed method, the entire domain is divided into two domains by a semicircle with a radius of 2 m.

To illustrate that the LBKM coefficient matrix is better conditioned than the BKM counterpart, Figure 5 presents the condition numbers of the BKM matrix versus the number of nodes for η = 1 and 1.5, and Figure 6 presents those of the LBKM matrix for the same η values. The coefficient matrices are generated for the finite domain shown in Figure 4, where the artificial boundary is assumed to satisfy the Neumann boundary condition. The BKM places nodes only on the boundary, whereas the LBKM distributes nodes throughout the entire finite domain. The parameter m for the LBKM is set to 20. The condition number of the LBKM matrix is smaller than that of the BKM matrix, confirming its superior conditioning.

Since the accuracy of the proposed method depends on the LBKM formulation and the semi-analytical formula in Eq (29), the impact of Eq (29) on the numerical results is first investigated here. Figure 7 plots the average relative errors of displacement u with respect to the number n_s. The incident angle θ_{inc} is π/2. The parameter η is set to 1, 2, and 8, while the number of discrete nodes in the finite domain for the LBKM is taken as N = 5628 and 9859. It can be seen that as the number n_s increases, the error decreases. When n_s reaches a certain value, the error no longer changes as n_s increases for different cases. This occurs because the error from the semi-analytical formula becomes smaller than that generated by the LBKM. Furthermore, as the frequency increases or when more discrete nodes are employed in the LBKM, a correspondingly larger value of n_s is necessary. Nevertheless, for cases where $\eta \le 8$, $n_s = 40$ ensures sufficient accuracy.

As the number of source points within the local influence domain Ξ_k is another factor influencing the numerical solution, its effect on the computational results is studied here. Figure 8 presents the condition number of the LBKM coefficient matrix for the finite domain versus m, obtained in the same manner as in Figure 6. The number of discrete nodes for the LBKM is set to 4003 and 5628. $\eta = 1$. It is observed that the condition number oscillates with m, which is due to the ill conditioning of $\boldsymbol{A}^{(k)}$ in Eq (11). Nevertheless, for $m \ge 18$, the condition number exhibits an overall decreasing trend as m increases, with relatively small oscillation amplitudes. Figure 9 provides the average relative errors of u computed by the LBKM versus the number of source points

m. The incident angle θ_{inc} is set to $\pi/2$. The finite domain is discretized into 4003 and 5268 nodes, respectively. Parameters n_s and η are set to 40 and 1, respectively. Obviously, for different cases, when $18 \le m \le 22$, the error difference is relatively small and lower than that for other values of m. According to the computational formula in Section 3, a larger m leads to higher computational cost. Considering both the effect of m on the condition number and on the numerical solution errors, m = 18 is an appropriate choice.

To further demonstrate the performance of the LBKM, it is compared here with the GFDM [20], localized method of fundamental solutions (LMFS) [39,40], and RPIM [41]. During computation, the GFDM is coupled with the PML. Specifically, the semi-infinite domain is truncated into a finite domain using a semicircle of radius 2 m, with a semicircular PML placed outside the truncated region. Each local influence domain in the GFDM consists of 12 nodes. Both the LMFS and RPIM are combined with the semi-analytical formulation in Eq (29), and the parameter n_s is set to 40. A semicircle of radius 2 m is used to divide the semi-infinite domain into two regions, and the interface conditions are handled in the same manner as for the LBKM. In the LMFS, a circle is employed to exactly enclose all nodes within a local subdomain. The auxiliary boundary of each local subdomain is another circle concentric with the enclosing circle, and the ratio of the radius of the auxiliary boundary to that of the enclosing circle is denoted by D. For the LMFS, the subdomain corresponding to each node contains its 20 nearest nodes, resulting in 21 nodes per local subdomain. Meanwhile, 12 nodes are uniformly distributed on the corresponding auxiliary boundary. As for the RPIM, interpolation within the local support domain is performed using the multiquadric function $\Phi(r) = \sqrt{r^2 + c^2}$ in conjunction with quadratic polynomial basis functions. The local support domain for any given node is constructed by identifying its 17 nearest neighbors, resulting in a total of 18 nodes (the node itself and its 17 neighbors) within the local support domain.

Before performing calculations using the GFDM, the influence of the PML thickness on the numerical results is examined, as shown in Figure 10. Parameter θ_{inc} is set to $\pi/2$, while parameter η takes the values 0.5 and 1. A total of 2574 nodes are distributed within the finite domain, while the node density in the PML is kept similar to that in the finite domain. The results indicate that when the PML thickness reaches or exceeds 0.8 m, the calculation error becomes nearly constant. However, increasing the PML thickness also increases the total number of GFDM nodes, thereby raising computational costs. Therefore, balancing computational efficiency against the need to avoid an overly thin PML (which could lead to inaccurate results), the PML thickness is set to 1 m in this example.

Table 1 gives the calculation errors and corresponding computation times for the LBKM and GFDM, while Tables 2 and 3 show the errors and computation times for the LMFS and RPIM, respectively. $\theta_{inc} = \pi/2$. The parameter η for all cases is set to 1. For the LBKM, the parameters are m = 18 and n_s = 40. The results show that both the LBKM and GFDM results converge stably to the analytical solution. When the calculation errors are comparable (GFDM: 3.38×10^{-3}, LBKM: 3.54×10^{-3}), the computation time of the LBKM (0.72 s) is approximately one-tenth that of the GFDM (6.90 s). Similarly, when the computation times are similar (GFDM: 1.39 s, LBKM: 1.64 s), the LBKM error (3.47×10^{-4}) is less than one-tenth of the GFDM error (8.17×10^{-3}). These results indicate that the LBKM outperforms the GFDM with PML. Furthermore, Table 2 shows that the LMFS with D = 3 yields results superior to those of the LBKM. However, with D = 1.5, the LMFS exhibits numerical instability. The RPIM with shape parameter c = 0.4 produces numerical solutions that converge to the analytical solution, but its performance is inferior to that of the LBKM. Moreover, the RPIM with c = 0.8 exhibits clear numerical instability.

Figure 11 plots the displacement distribution along the boundary computed by the LBKM with 5628 nodes. m = 18, and n_s = 40. $\eta = 2$. The agreement between numerical and analytical solutions demonstrates the validity of the proposed method.

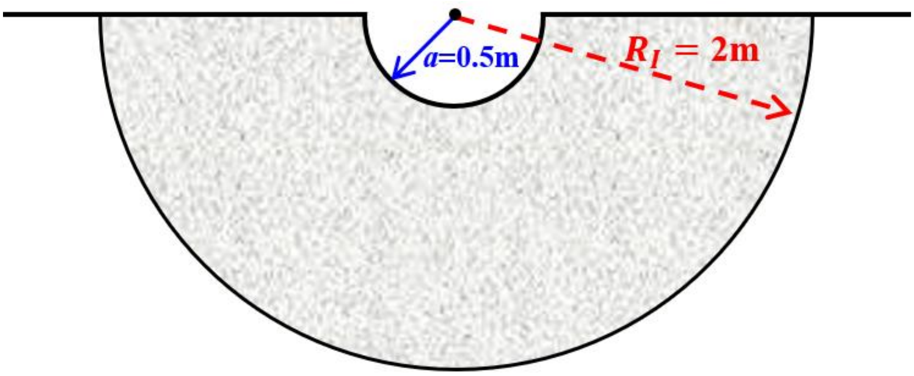

Figure 4. Sketch of a single semicircular canyon.

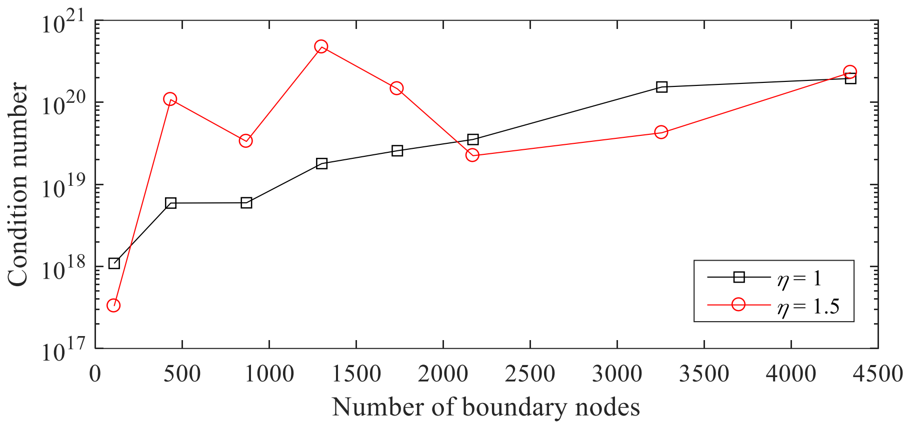

Figure 5. Condition number of the BKM coefficient matrix versus number of boundary nodes.

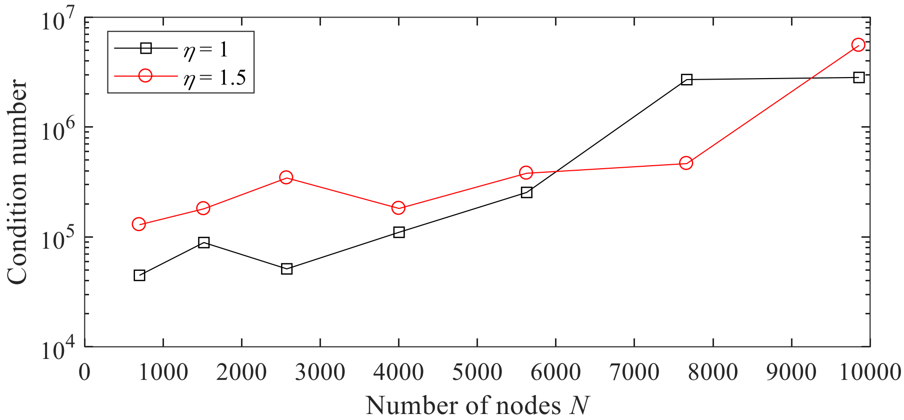

Figure 6. Condition number of the LBKM coefficient matrix versus number of nodes in the finite domain.

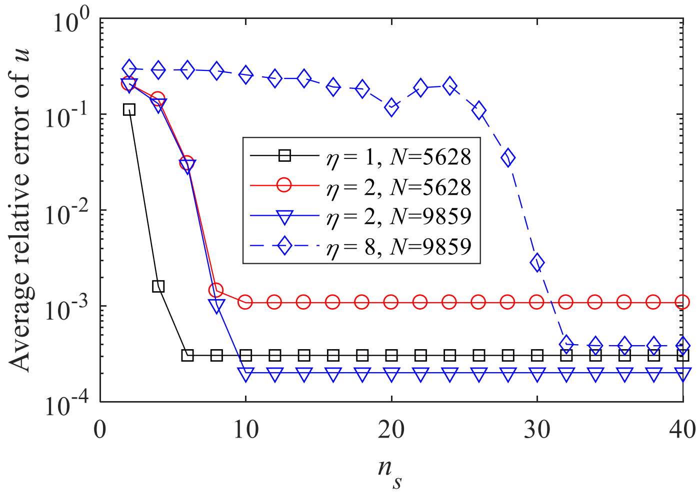

Figure 7. The errors of u versus the number n_s obtained by the LBKM.

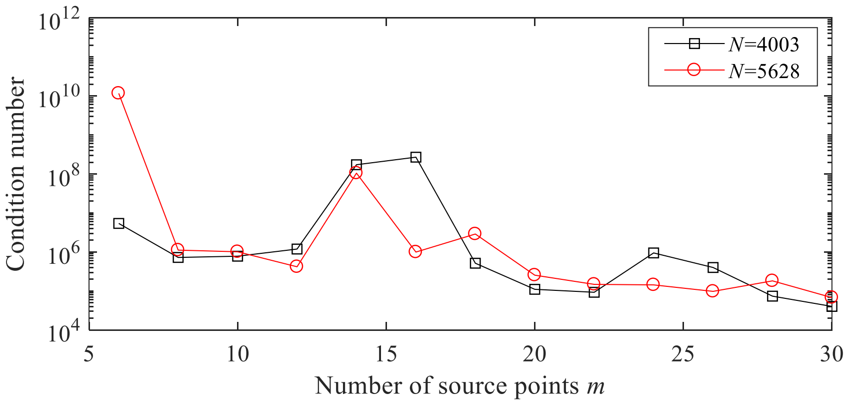

Figure 8. Condition number of the LBKM coefficient matrix versus number of source points in the local influence domain for $\eta = 1$.

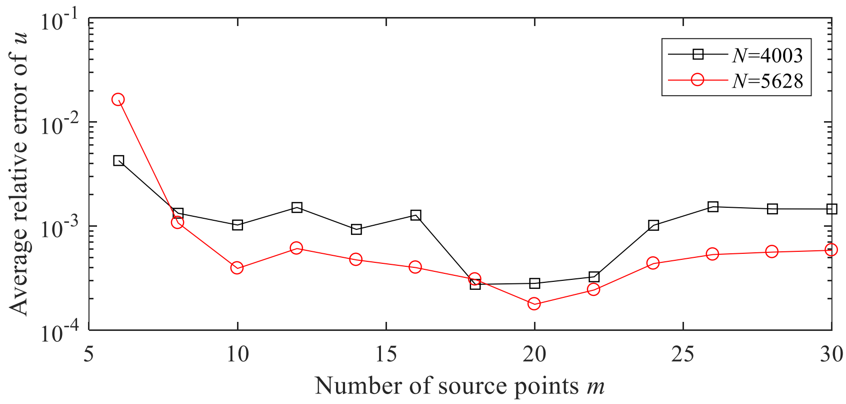

Figure 9. The errors versus m obtained by the LBKM for $\eta = 1$.

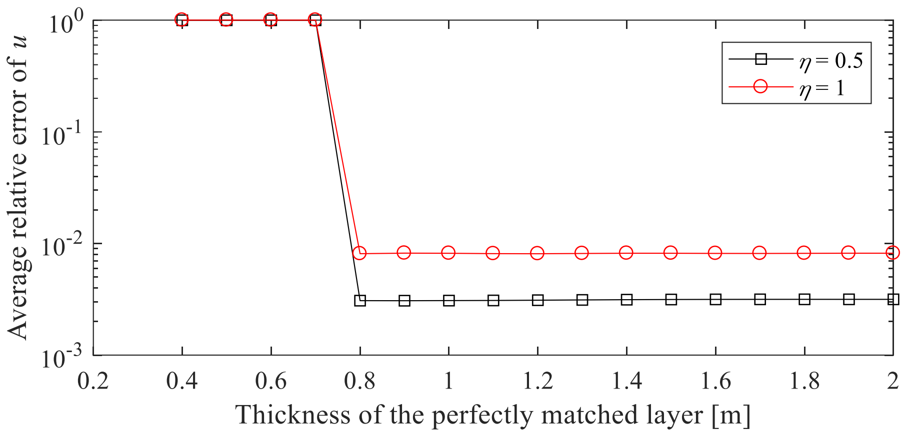

Figure 10. Errors versus thickness of the PML for the GFDM.

Table 1. Average relative error of u obtained by the LBKM and GFDM for η = 1.

LBKM			GFDM		
Number of nodes	$arerr(u)$	CPU Time (s)	Number of nodes	$arerr(u)$	CPU Time (s)
698	0.014	0.27	1661	0.043	0.52
2574	3.54e-3	0.72	6070	8.17e-3	1.39
5628	3.47e-4	1.64	13226	3.38e-3	6.90
9859	2.61e-4	2.84	23132	1.83e-3	31.1

Table 2. Average relative error of u obtained by the LMFS for η = 1.

Number of nodes	LMFS (D = 1.5)		LMFS (D = 3)	
	$arerr(u)$	CPU Time (s)	$arerr(u)$	CPU Time (s)
698	0.041	0.22	0.028	0.21
2574	8.07e-4	0.56	7.91e-4	0.74
5628	4.07e-4	1.31	1.65e-4	1.41
9859	9.83e-4	2.59	5.58e-5	2.53

Table 3. Average relative error of u obtained by the RPIM for η = 1.

Number of nodes	RPIM (c = 0.4)		RPIM (c = 0.8)	
	$arerr(u)$	CPU Time (s)	$arerr(u)$	CPU Time (s)
698	0.017	0.31	0.031	0.32
2574	4.09e-3	0.89	0.019	0.87
5628	1.53e-3	1.74	1.50e-3	1.77
9859	4.3e-4	2.92	0.25	3.29

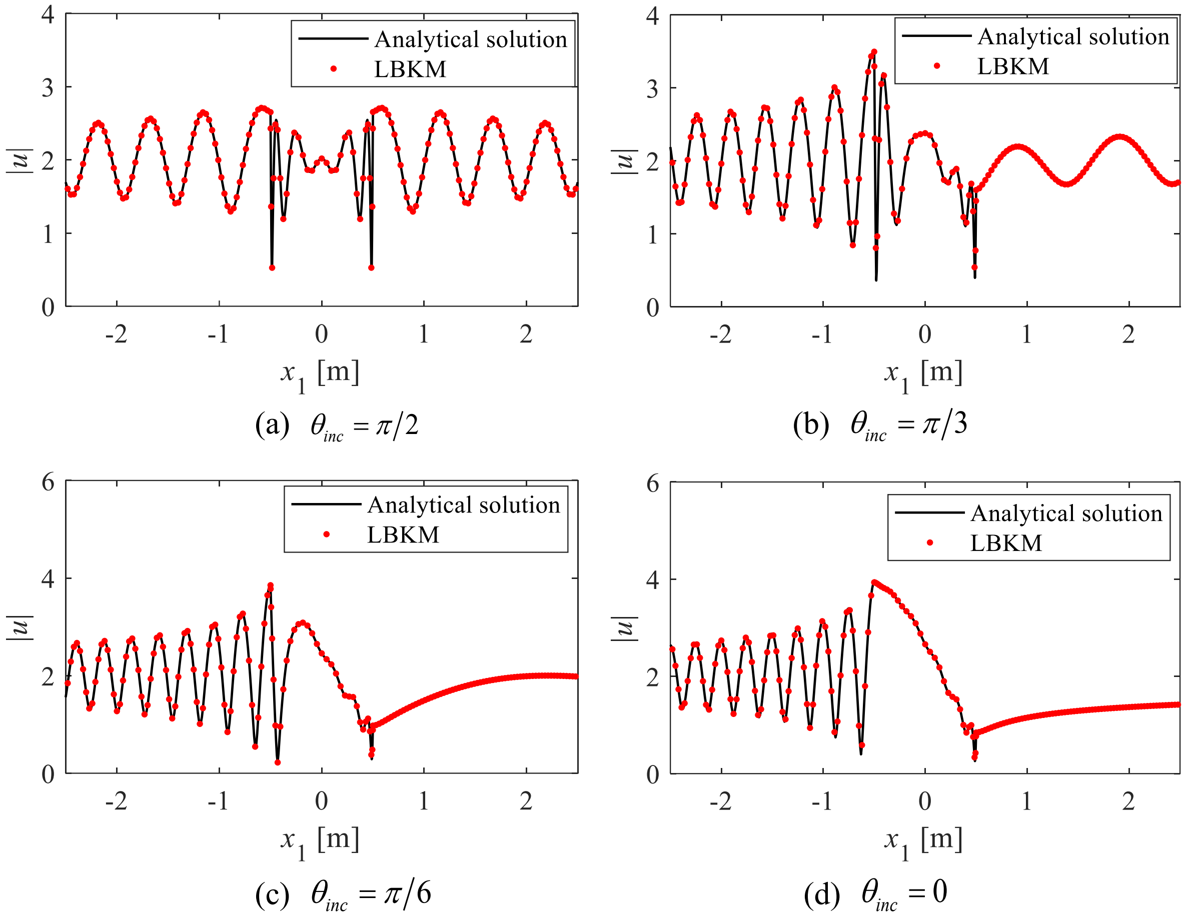

Figure 11. Ground surface displacement computed using the LBKM and the analytical solution formula ($\eta = 2$).

4.1.2. Two semi-circular canyons

To further evaluate the effectiveness of the LBKM, the case of two semi-circular canyons is considered next. The centers of the canyons are located at $(0.75, 0)$ and $(-0.75, 0)$, respectively, and both have a radius of $a = 0.5$ m. In the LBKM, the semi-infinite domain is truncated into a finite domain and an infinite domain by using a semicircle of radius 2 m. Since the analytical solution is difficult to obtain, the results computed by the FEM are taken as the reference solution. In the FEM simulation, the semi-infinite domain is truncated into a finite domain by a semicircle of radius 5 m, and a PML of thickness 1m is placed outside this domain. The entire domain is discretized into 685660 triangular elements.

Figure 12 shows the average relative error of u as a function of m, with $n_s = 40$. The incident angle θ_{inc} is $\pi/2$. The numbers of discrete nodes used for the LBKM are $N = 3783$ and $N = 5349$. It can be seen from the figure that the range [18, 24] is a suitable choice for m, which is consistent with the case of a single canyon.

Table 4 compares the errors and the corresponding computation time of the LBKM and the GFDM. The incident angle θ_{inc} is set to $\pi/2$. In the GFDM calculations, each local influence domain contains 12 nodes, and the semi-infinite domain is truncated into a finite domain by a semicircle of radius 2 m, with a PML of thickness 1m placed outside the finite domain. In the LBKM calculations, m = 18 and n_s = 40. The observed phenomena are similar to those in Table 1, once again demonstrating that the LBKM outperforms the GFDM.

Figure 13 provides the ground surface displacement distributions calculated by the FEM and the LBKM. For the LBKM, 5349 nodes are employed with m = 18 and n_s = 40. $\eta = 1$. The results from the two methods agree well, further confirming the validity of the LBKM for SH-wave scattering problems in a semi-infinite domain.

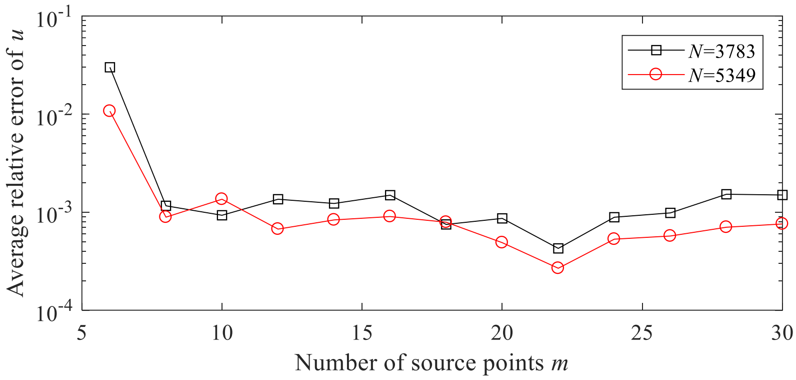

Figure 12. Errors versus m obtained by the LBKM for the case of two canyons ($\eta = 1$).

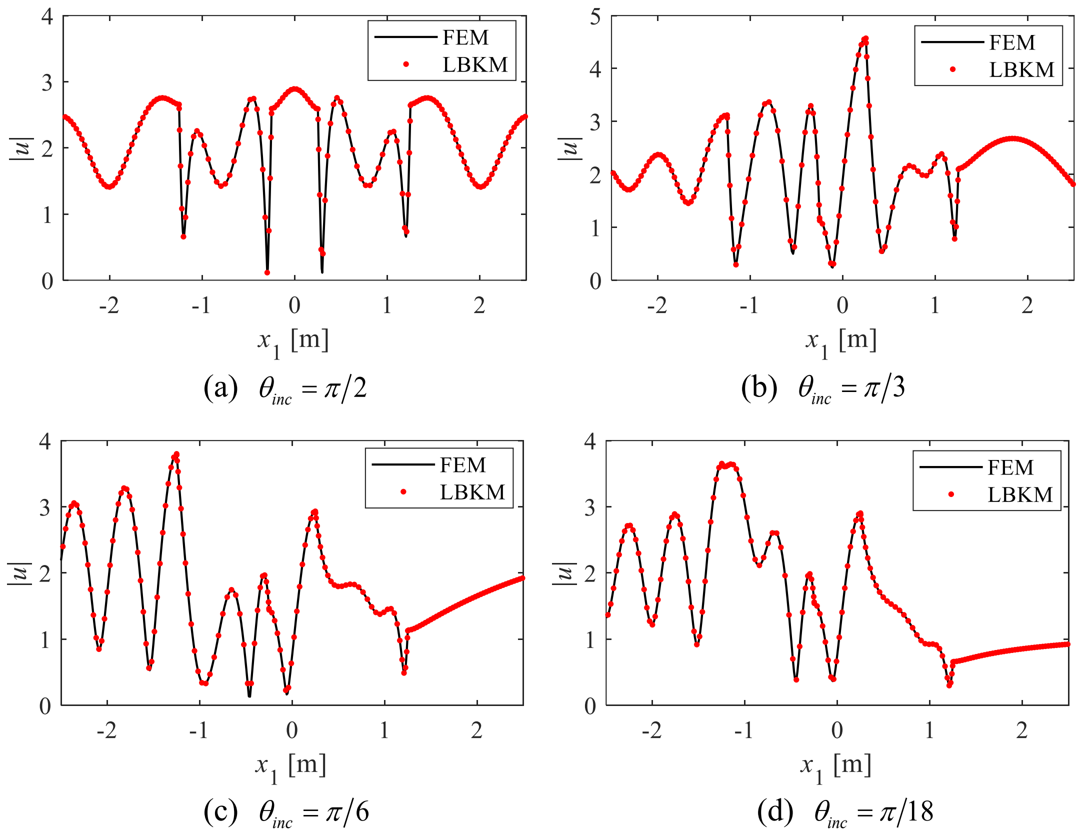

Figure 13. The displacement on the boundary obtained using the LBKM and FEM for the case of two canyons ($\eta = 1$).

Table 4. Average relative error of u obtained by the LBKM and GFDM for the case of two canyons (η = 1).

LBKM			GFDM		
Number of nodes	$arerr(u)$	CPU Time (s)	Number of nodes	$arerr(u)$	CPU Time (s)
687	0.012	0.24	1650	0.048	0.39
2468	1.48e-3	0.67	5964	0.013	1.38
5349	7.89e-4	1.46	12947	5.88e-3	6.38
9346	4.27e-4	2.59	22619	4.19e-3	28.8

4.2. Underground twin tunnels

As illustrated in Figure 14 (a = 0.4 m), the scattering of SH waves by two underground tunnels is investigated. To obtain the reference solutions using the FEM, the computational domain was truncated as a semicircular region with a radius of 6 m. The PML of 1m thickness was applied at the artificial boundary, and a total of 84908 triangular elements were employed for the FEM. The radius of boundary Γ_I (Figure 14) was set to 2.5 m, and 3701 nodes are distributed in the finite domain for the LBKM. The parameters are m =18 and n_s = 40.

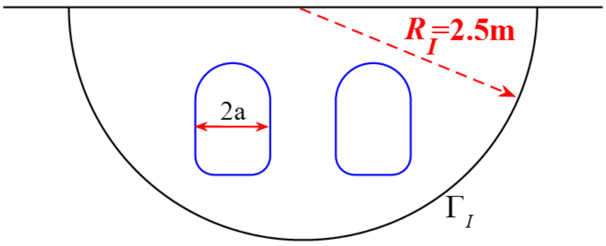

Figure 14. Sketch of two underground tunnels.

In Figures 15–17, the displacement distributions on the upper boundary calculated by the LBKM and FEM are given for different values of the incident angle and frequency, respectively. The agreement between the two methods confirms the accuracy of the proposed method. Additionally, the results in the figures clearly show that the ground displacements are amplified due to the influence of the underground tunnel.

Figure 18 shows the distributions of u_{sc} computed by the LBKM and FEM for various incident angles. The parameter η is set to 1. As observed in the figure, the absence of visible discrepancies between the results from both computational methods demonstrates that the proposed method can accurately simulate the scattered field distribution within the domain.

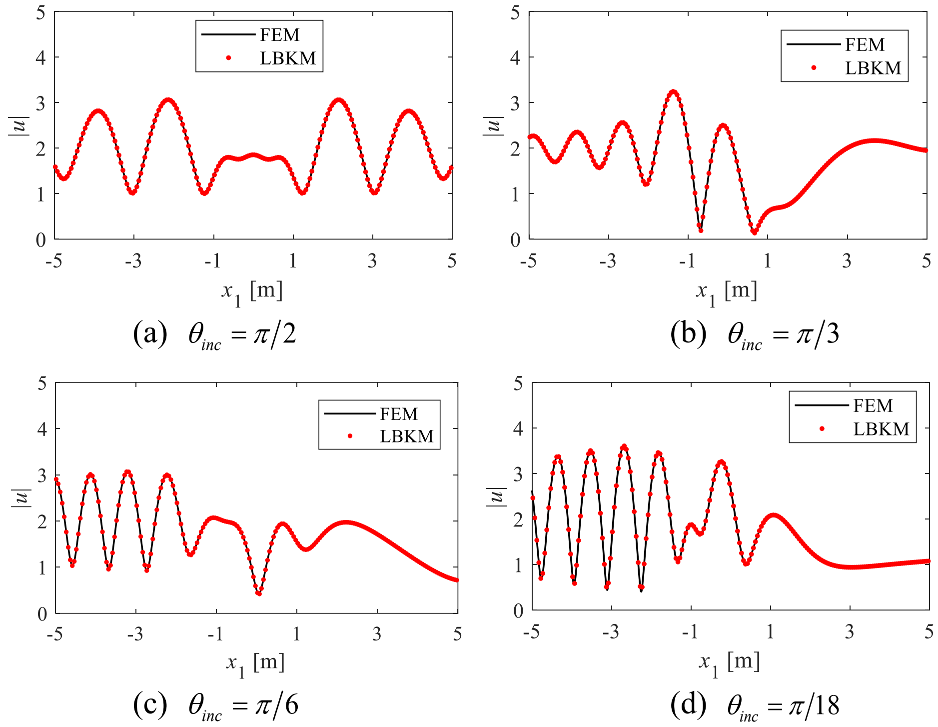

Figure 15. Displacement distribution on the boundary $x_2 = 0$ computed by the LBKM and FEM for $\eta = 0.5$.

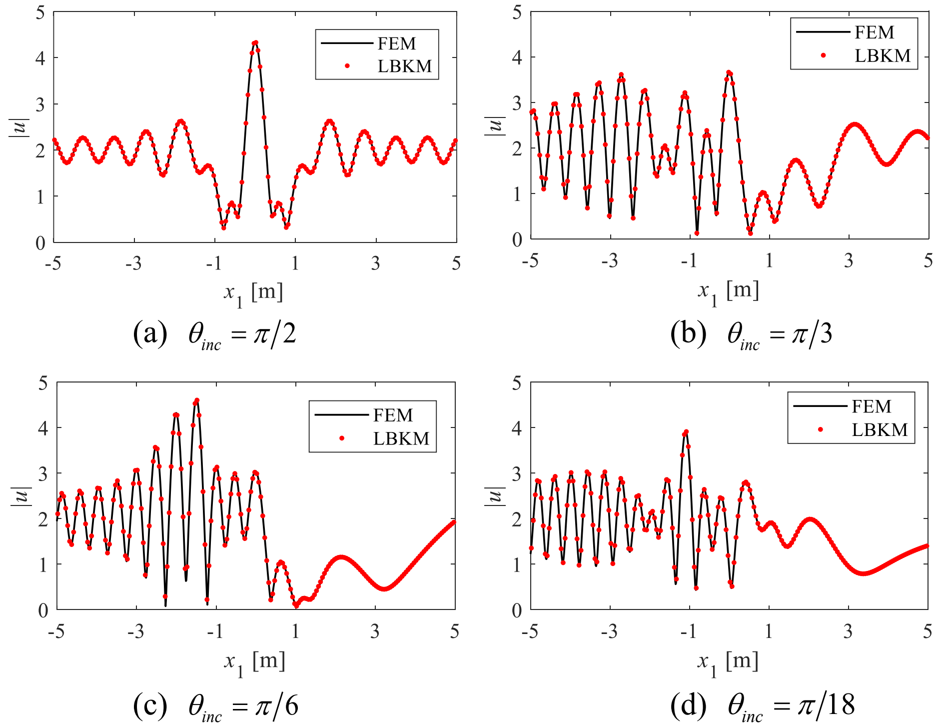

Figure 16. Displacement distribution on the boundary $x_2 = 0$ computed by the LBKM and FEM for $\eta = 1$.

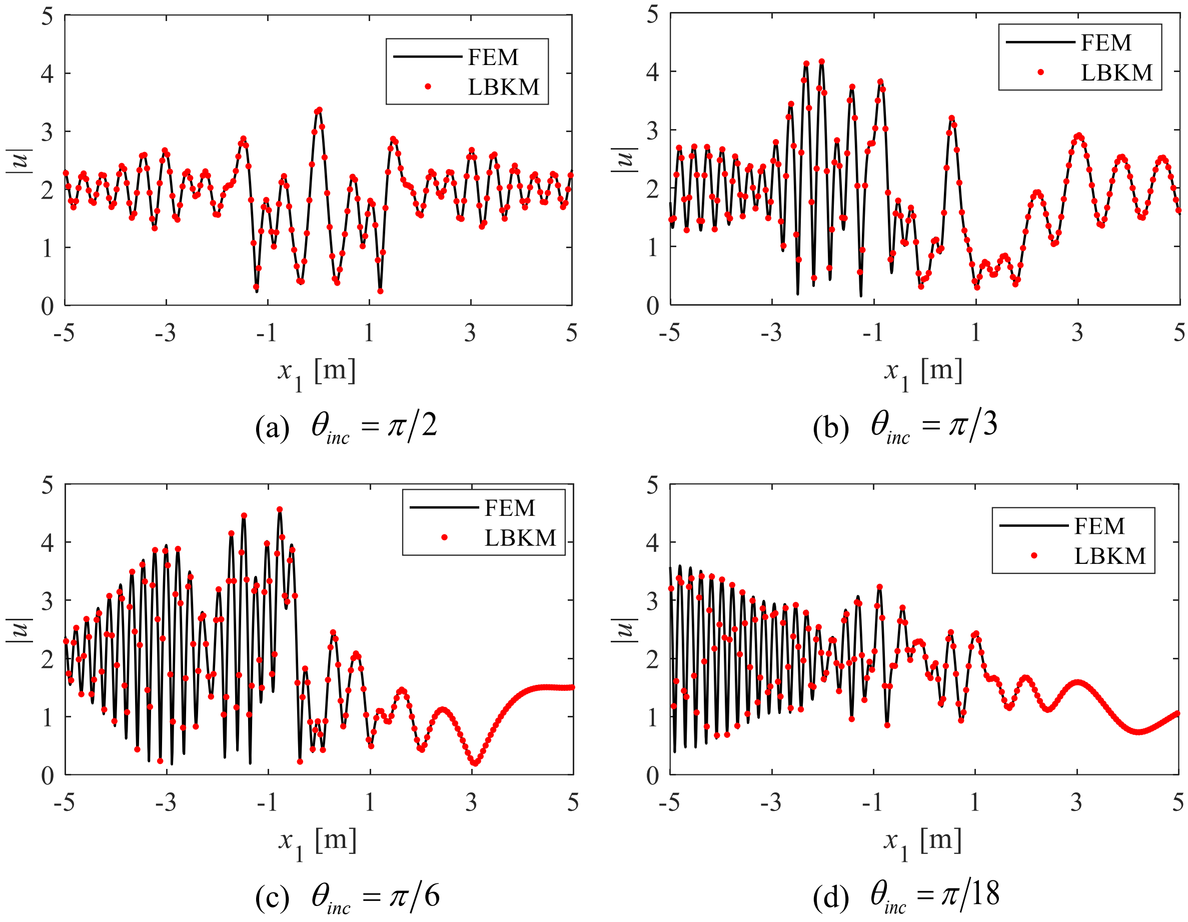

(a) $\theta_{inc} = \pi/2$ (b) $\theta_{inc} = \pi/3$

(c) $\theta_{inc} = \pi/6$ (d) $\theta_{inc} = \pi/18$

Figure 17. Displacement distribution on the boundary $x_2 = 0$ computed by the LBKM and FEM for $\eta = 2$.

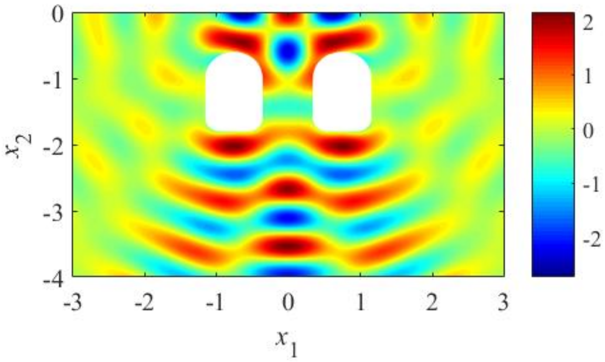

(a) LBKM ($\theta_{inc} = \pi/2$)

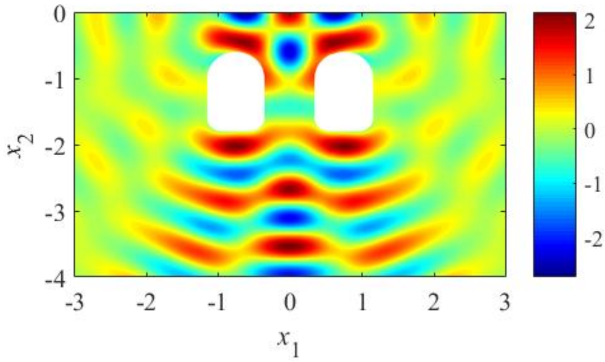

(b) FEM ($\theta_{inc} = \pi/2$)

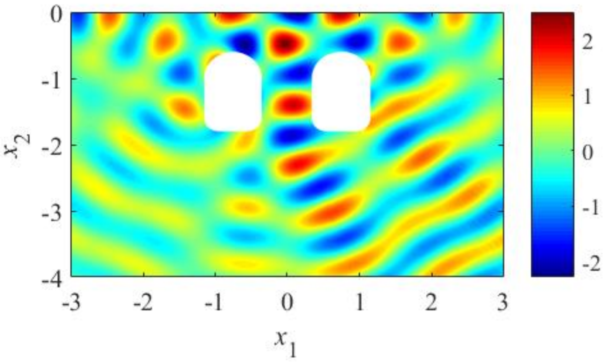

(c) LBKM ($\theta_{inc} = \pi/3$)

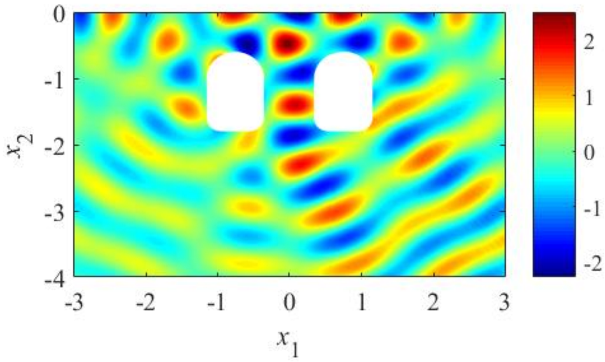

(d) FEM ($\theta_{inc} = \pi/3$)

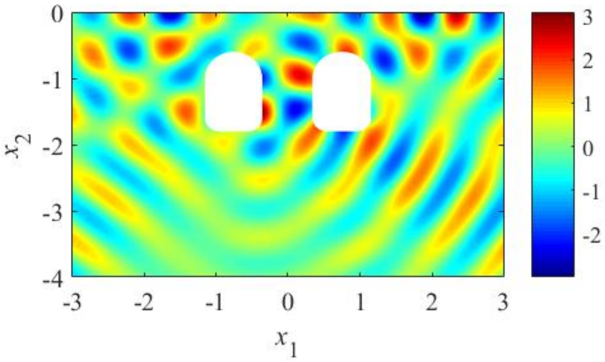

(e) LBKM ($\theta_{inc} = \pi/6$)

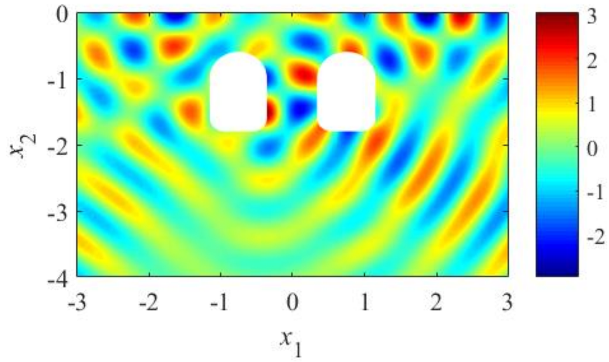

(f) FEM ($\theta_{inc} = \pi/6$)

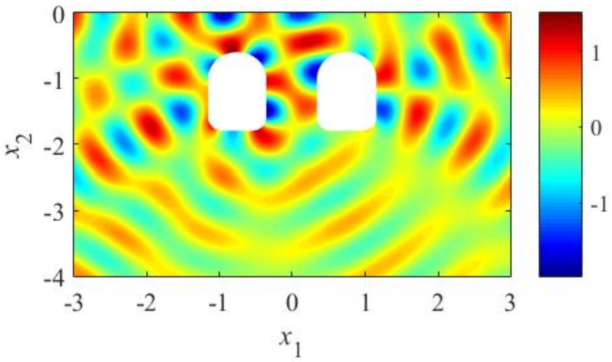

(g) LBKM ($\theta_{inc} = \pi/18$)

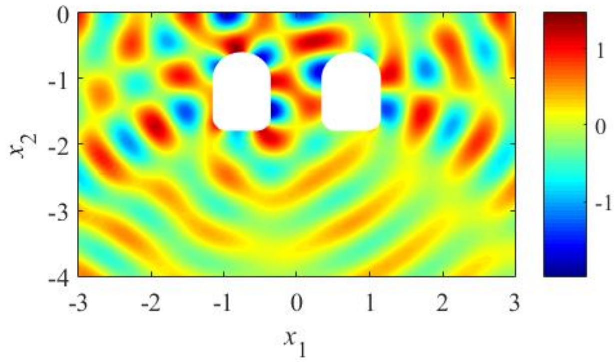

(h) FEM ($\theta_{inc} = \pi/18$)

Figure 18. Distribution of Re(u_{sc}) within the domain obtained by the LBKM and FEM for $\eta = 1$.

4.3. Multiple circular inclusions

In the last example, the problem of a semi-infinite plane containing four circular inclusions, each with a radius of 0.25 m, centered at (-0.5, -0.5), (0.5, -0.5), (-0.5, -1.5), and (0.5, -1.5), as illustrated in Figure 19, is analyzed. Two different material parameters are considered:

Case 1: $\bar{\mu} = 15$ GPa, $\bar{\rho} = 2500$ kg/m^3;

Case 2: $\bar{\mu} = 25$ GPa, $\bar{\rho} = 3000$ kg/m^3.

Because analytical solutions are unavailable, the FEM reference solution was obtained by truncating the computational domain into a semicircular domain with 5 m radius, and implementing a PML of 1m thickness. Furthermore, 251860 triangular elements are employed. For the LBKM, the radius of boundary Γ_I (Figure 19) was set to 2 m. m = 18, and n_s = 40.

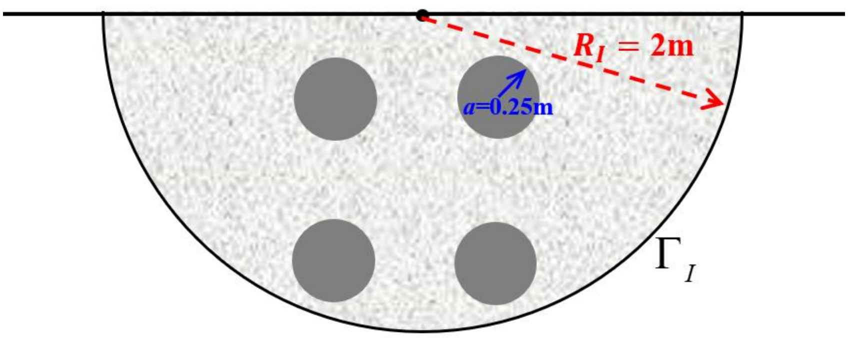

Figure 19. Semi-infinite domain with inclusions.

Figure 20 shows the displacement distribution on the boundary for different incident angles when η = 0.5. In this case, 400 nodes were distributed within the inclusion and 2120 nodes were arranged outside the inclusion. Obviously, the LBKM results agree well with the FEM results. Figure 21 plots the SH-wave propagation under vertical incidence computed by both the LBKM and FEM at different frequencies. Here, 1288 nodes were distributed within the inclusion and 7824 nodes were arranged outside the inclusion. The consistent agreement between the two methods demonstrates the capability of the proposed approach to accurately describe wave propagation within the domain.

Table 5 provides the displacement amplitude at (1,0) for η = 3 computed using the LBKM for the first case, where h is the spacing between adjacent internal nodes along the x_1 or x_2 axis. A systematic refinement with a constant ratio of 1.5 is performed. From h = 1/24 to 1/36, the relative change is 4.11%, indicating that the coarsest node distribution is insufficient. Further refinement to h = 1/54 yields a change of only 0.39%, and refinement to h = 1/81 gives 0.22%. Both values are well below 1%, demonstrating that the solution has converged and become essentially independent of the node density.

Figures 22 and 23 show the displacement distribution on the boundary and within the domain for the second case, respectively. The distribution and number of nodes in the finite domain used for Figure 22 follow those in Figure 20, and those for Figure 23 follow those in Figure 21. A comparison with the results in Figures 20 and 21 reveals that the scattering characteristics of SH waves exhibit significant differences when the material properties of the inclusions are different. Nevertheless, the consistency between the LBKM and FEM results further confirms the validity of the proposed method in analyzing SH-wave scattering by multiple inclusions.

Table 6 presents the displacement amplitude at (1,0) for the second case under the same refinement. The relative changes between consecutive refinement levels are 0.81%, 0.079%, and 0.099%, respectively. Despite a slight fluctuation in the last refinement step, the overall variation remains well below 1%. This further confirms the robustness of the LBKM.

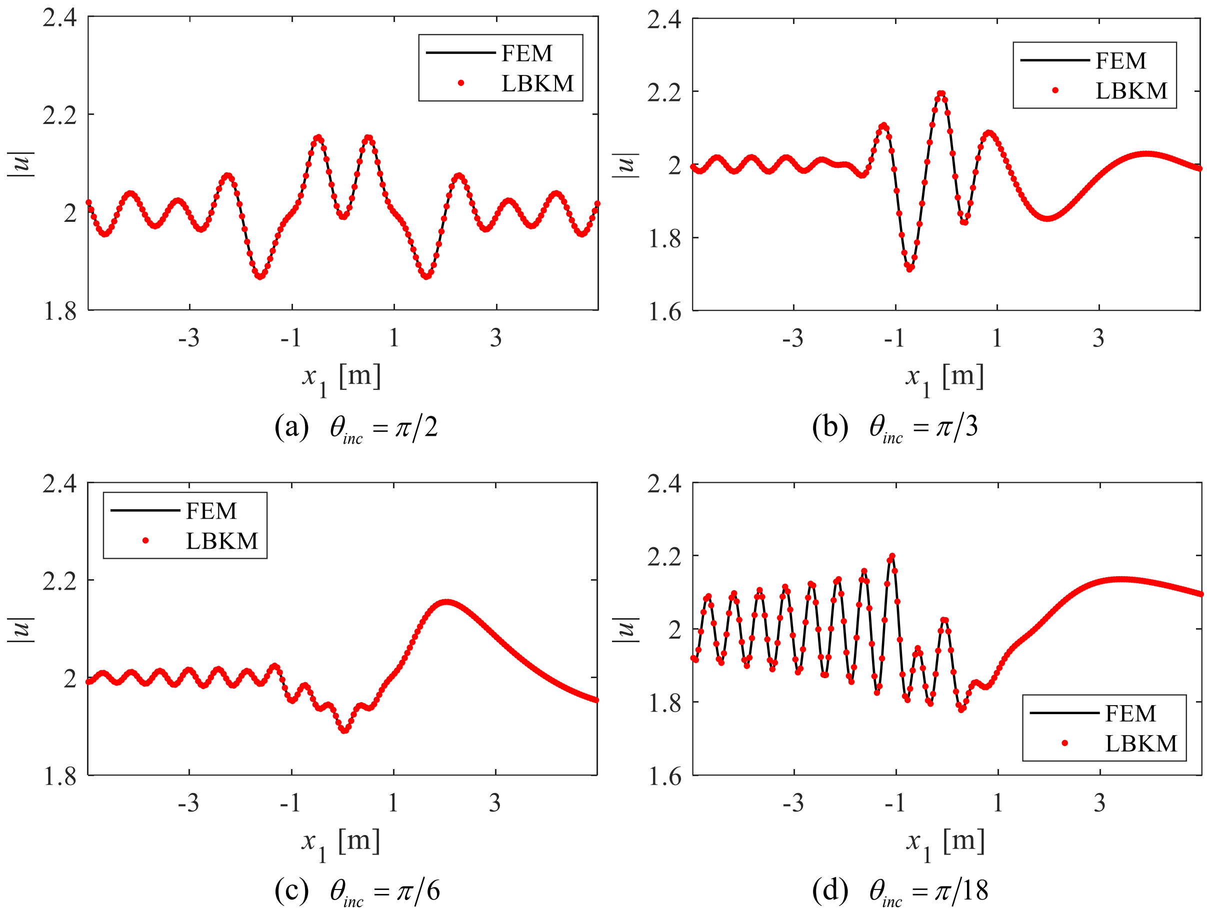

Figure 20. The distribution of u ($\eta = 0.5$) on the boundary computed by the LBKM and FEM for the first case.

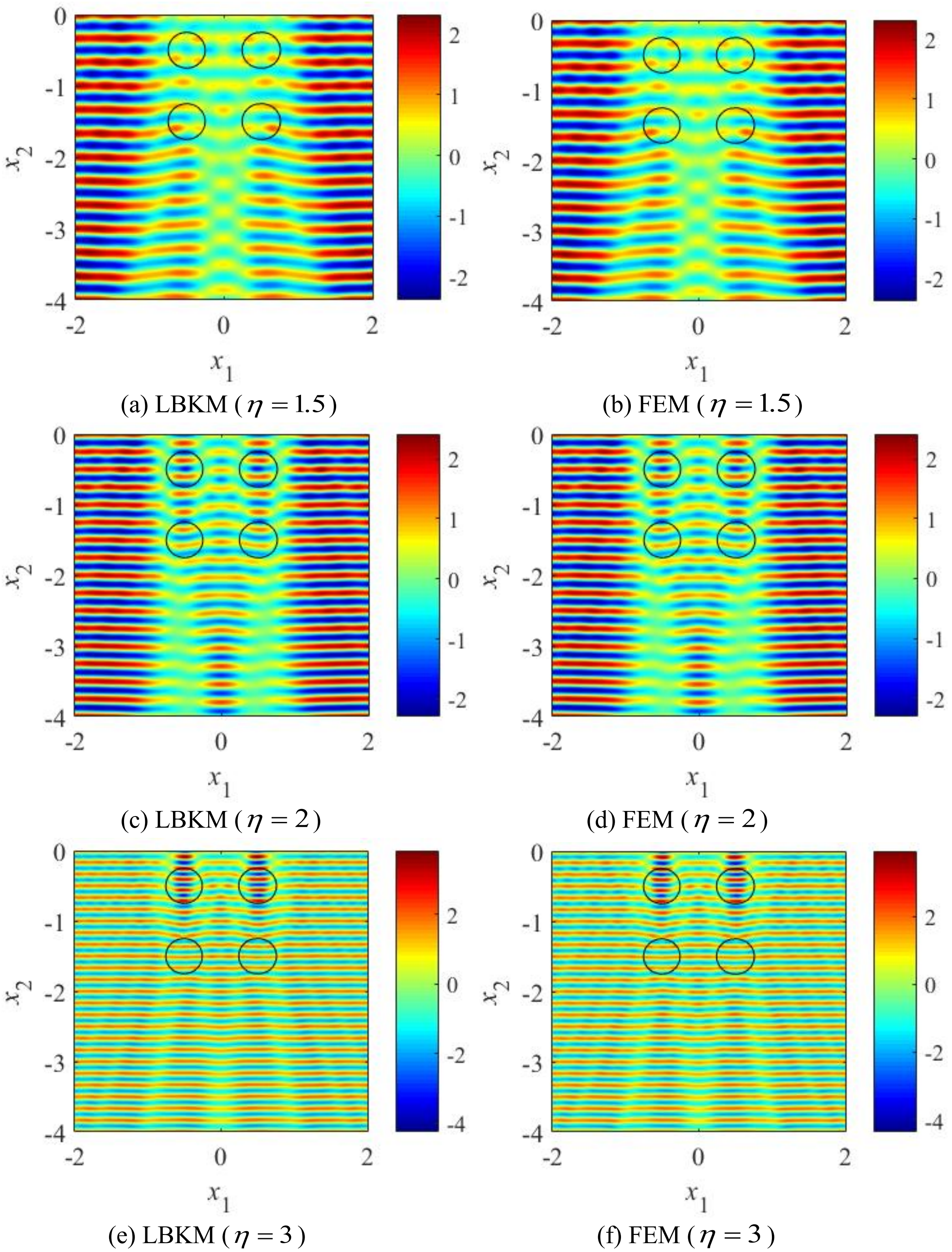

Figure 21. Contour plots of Re(u) computed by the LBKM and FEM with $\theta_{inc} = \pi/2$ for the first case.

Table 5. The displacement amplitude at (1,0) calculated by the LBKM for the first case varies with h when $\eta = 3$ and $\theta_{inc} = \pi/2$.

Number k	h	Relative refinement ratio	Number of nodes inside inclusion	Number of nodes outside inclusion	Displacement amplitude $u_A = \|u\|$	$\frac{\|u_{A,k} - u_{A,k-1}\|}{\|u_{A,k}\|}$
1	1/24	-	656	3612	1.801009	-
2	1/36	1.5	1288	7824	1.729770	4.11%
3	1/54	1.5	2776	17086	1.722978	0.39%
4	1/81	1.5	5820	37702	1.726744	0.22%

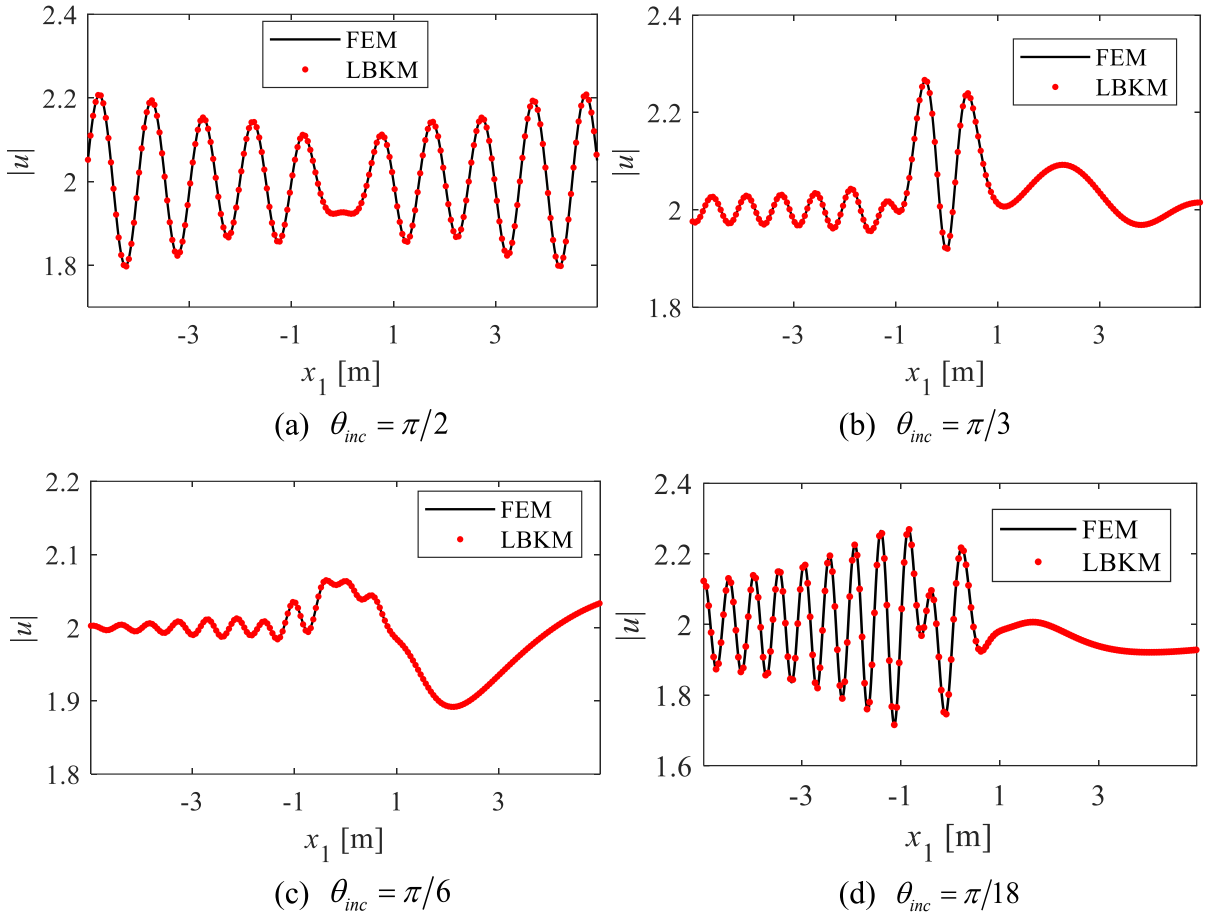

Figure 22. The distribution of u ($\eta = 0.5$) on the boundary computed by the LBKM and FEM for the second case.

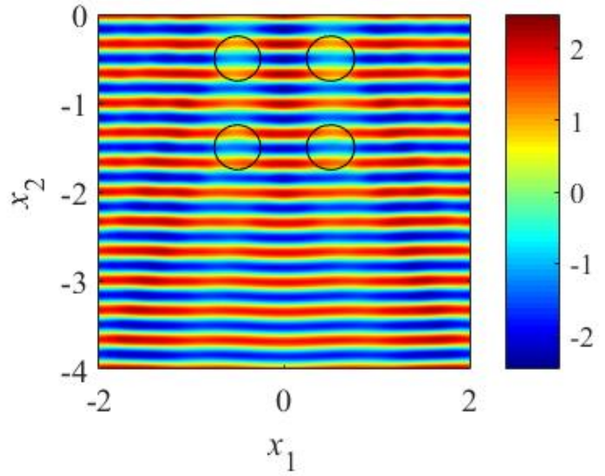

(a) LBKM ($\eta = 1.5$)

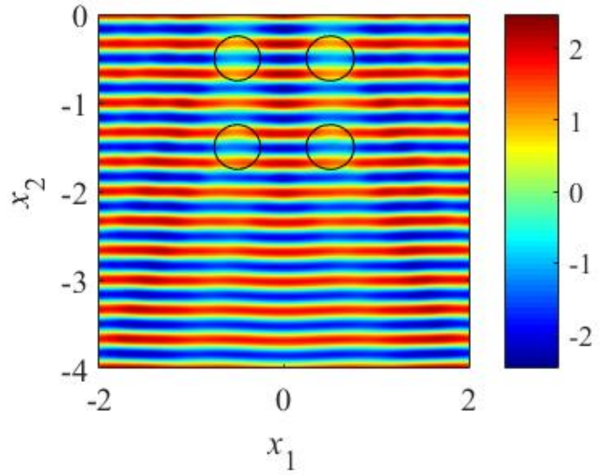

(b) FEM ($\eta = 1.5$)

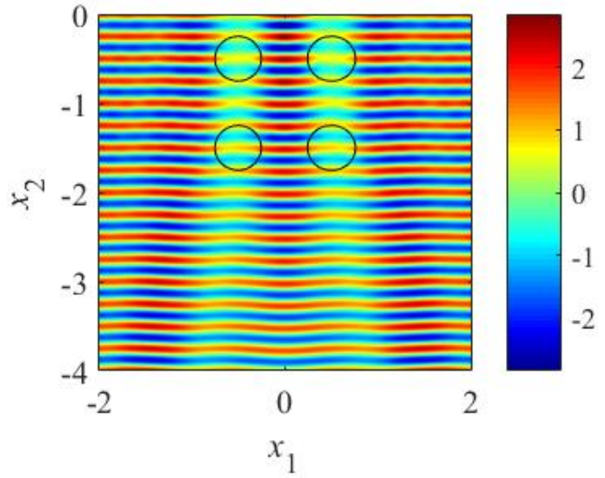

(c) LBKM ($\eta = 2$)

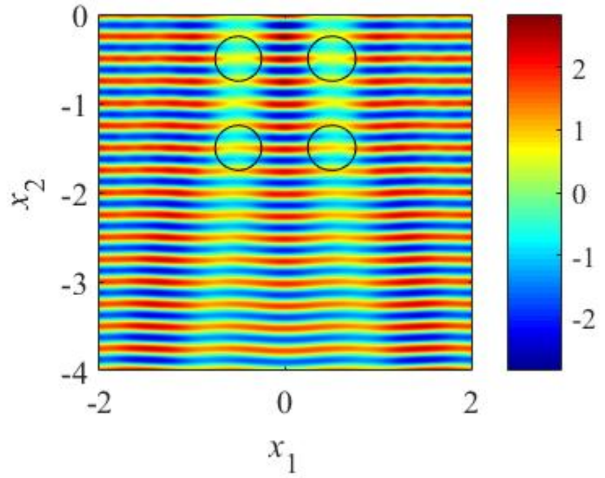

(d) FEM ($\eta = 2$)

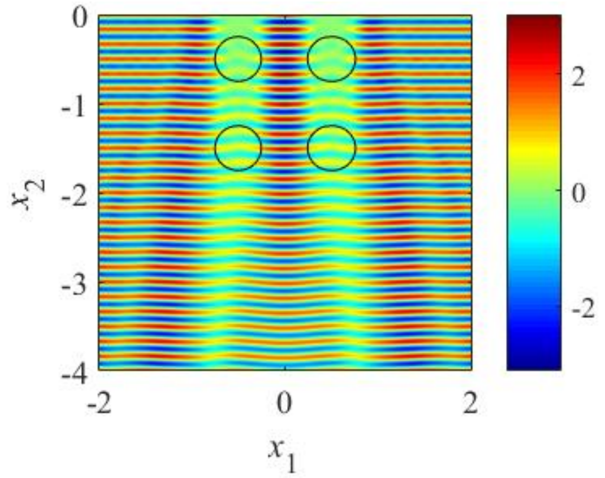

(e) LBKM ($\eta = 3$)

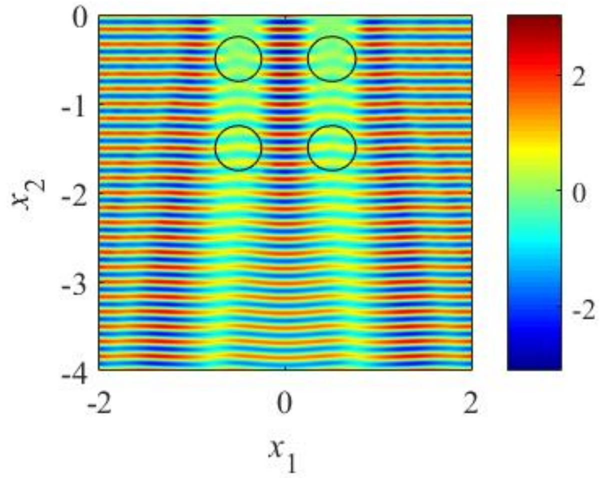

(f) FEM ($\eta = 3$)

Figure 23. Contour plots of Re(u) computed by the LBKM and FEM with $\theta_{inc} = \pi/2$ for the second case.

Table 6. The displacement amplitude at (1,0) calculated by the LBKM for the second case varies with h when $\eta = 3$ and $\theta_{inc} = \pi/2$.

Number k	h	Relative refinement ratio	Number of nodes inside inclusion	Number of nodes outside inclusion	Displacement amplitude $u_A = \lvert u \rvert$	$\frac{\lvert u_{A,k} - u_{A,k-1} \rvert}{\lvert u_{A,k} \rvert}$
1	1/24		656	3612	2.515102	
2	1/36	1.5	1288	7824	2.494969	0.81%
3	1/54	1.5	2776	17086	2.492995	0.079%
4	1/81	1.5	5820	37702	2.490511	0.099%

5. Conclusions

This paper applies the LBKM to analyze SH-wave scattering problems. The problem is decomposed into an internal finite domain problem, which is solved using the LBKM, and an external infinite domain problem, where the field variables are approximated by a semi-analytical formulation satisfying the governing equations and the boundary conditions on the horizontal ground surface.

Numerical experiments were conducted to evaluate the computational accuracy and effectiveness of the proposed method. The results demonstrate that the LBKM outperforms the GFDM with PML. Specifically, when a sufficiently large number of nodes are used, the LBKM requires approximately one-tenth of the computation time needed by the GFDM to achieve the same level of accuracy. Conversely, for comparable computation times, the error of the LBKM is less than one-tenth of that of the GFDM. Furthermore, in contrast to the LMFS, the LBKM yields results that converge stably to the analytical solution, owing to the absence of the auxiliary boundary. Similarly, compared with the RPIM, the LBKM shows superior performance and more stable convergence to the analytical solution.

Validation against reference solutions obtained using the FEM confirms its capability to effectively solve various SH-wave scattering problems. In particular, the method can accurately describe the wave propagation process involving underground tunnels and inclusions of diverse materials under varying conditions such as incident angles and frequencies.

Future work will extend the proposed LBKM to stochastic SH-wave scattering problems by integrating the uncertainty quantification framework [42]. In addition, the LBKM will be applied to elastic wave problems and wave propagation in porous media [43].

Author contributions

Shuwei Zhang: Methodology, Software, Validation, Visualization, Writing – original draft. **Shuihuai Yang:** Methodology, Software, Validation, Writing – original draft. **Xing Wei:** Conceptualization, Methodology, Supervision, Writing – review & editing. **Haowen Wu:** Methodology, Software, Validation. **Linlin Sun:** Conceptualization, Methodology, Software, Supervision, Writing – review & editing. All authors have read and approved the final version of the manuscript for publication.

Use of Generative-AI tools declaration

The authors declare they have not used Artificial Intelligence (AI) tools in the creation of this article.

Acknowledgments

This work was supported by the National Natural Science Foundation of China (Grant Nos. 11602114), and Nantong Natural Science Foundation of China (Grant Nos. JC2024009, JC2024008).

Conflict of interest

The authors declare that we have no known competing financial interests or personal relationships that could have appeared to influence the work reported in this paper.

References

1. M. I. Todorovska, V. W. Lee, Surface motion of shallow circular alluvial valleys for incident plane SH waves-analytical solution, *Soil Dyn. Earthquake Eng.*, **10** (1991), 192–200. https://doi.org/10.1016/0267-7261(91)90033-v
2. C. Smerzini, J. Avilés, F. J. Sánchez-Sesma, R. Paolucci, A. Santini, N. Moraci, Analytical solutions for the seismic response of underground structures under SH wave propagation, *AIP Conf. Proc.*, **1020** (2008), 674–683. https://doi.org/10.1063/1.2963900
3. N. Zhang, X. Chen, Y. Gao, D. Dai, Analytical solution to scattering of SH waves by a circular lined tunnel embedded in a semi–circular alluvial valley in an elastic half–space, *Tunn. Undergr. Space Technol.*, **106** (2020), 103615. https://doi.org/10.1016/j.tust.2020.103615
4. T. Sun, P. Wang, G. Zhang, Y. Chai, Transient analyses of wave propagations in nonhomogeneous media employing the novel finite element method with the appropriate enrichment function, *Comput. Math. Appl.*, **129** (2023), 90–112. https://doi.org/10.1016/j.camwa.2022.10.004
5. C. Xu, Q. Liu, J. Wu, P. Deng, P. Liu, H. Zhang, Numerical study on P-wave propagation across the jointed rock masses by the combined finite-discrete element method, *Comput. Geotech.*, **142** (2022), 104554. https://doi.org/10.1016/j.compgeo.2021.104554
6. P. Destuynder, L. Hervella-Nieto, P. M. López-Pérez, J. Orellana, A. Prieto, A modal-based Partition of Unity Finite Element Method for elastic wave propagation problems in layered media, *Comput. Struct.*, **265** (2022), 106759. https://doi.org/10.1016/j.compstruc.2022.106759
7. L. Huang, X. Liu, Z. Liu, T. Ai, Scattering of seismic waves by reef sites in saturated layered sea areas-simulated using the indirect boundary element method, *Soil Dyn. Earthquake Eng.*, **183** (2024), 108804. https://doi.org/10.1016/j.soildyn.2024.108804
8. L. Huang, Z. Liu, C. Wu, J. Liang, Q. Pei, A three-dimensional indirect boundary integral equation method for the scattering of seismic waves in a poroelastic layered half-space, *Eng. Anal. Boundary Elem.*, **135** (2022), 167–181. https://doi.org/10.1016/j.enganabound.2021.11.012

9. L. Chen, H. Lian, Y. Xu, S. Li, Z. Liu, E. Atroshchenko, et al., Generalized isogeometric boundary element method for uncertainty analysis of time-harmonic wave propagation in infinite domains, *Appl. Math. Model.*, **114** (2023), 360–378. https://doi.org/10.1016/j.apm.2022.09.030
10. M. Rasht-Behesht, C. Huber, K. Shukla, G. E. Karniadakis, Physics-informed neural networks (PINNs) for wave propagation and full waveform inversions, *J. Geophys. Res.: Solid Earth*, **127** (2022), e2021JB023120. https://doi.org/10.1029/2021JB023120
11. L. Qiu, Y. Wang, Y. Gu, Q. H. Qin, F. Wang, Adaptive physics-informed neural networks for dynamic coupled thermo-mechanical problems in large-size-ratio functionally graded materials, *Appl. Math. Model.*, **140** (2025), 115906. https://doi.org/10.1016/j.apm.2024.115906
12. J. Li, L. Zhang, S. Cai, N. Li, Regularized singular boundary method for calculating wave forces on three-dimensional large offshore structure, *Appl. Math. Lett.*, **149** (2024), 108931. https://doi.org/10.1016/j.aml.2023.108931
13. L. Sun, Z. Fu, Z. Chen, A localized collocation solver based on fundamental solutions for 3D time harmonic elastic wave propagation analysis, *Appl. Math. Comput.*, **439** (2023), 127600. https://doi.org/10.1016/j.amc.2022.127600
14. X. Wei, W. Luo, 2.5D singular boundary method for acoustic wave propagation, *Appl. Math. Lett.*, **112** (2021), 106760. https://doi.org/10.1016/j.aml.2020.106760
15. M. Xiang, H. Qi, J. Guo, Technical note: the anti-plane scattering of SH waves by the non-circular cavity in an infinite strip, *J. Earthquake Eng.*, **26** (2022), 3228–3245. https://doi.org/10.1080/13632469.2020.1793843
16. Z. Ge, Simulation of the seismic response of sedimentary basins with constant-gradient velocity along arbitrary direction using boundary element method: SH case, *Earthquake Sci.*, **23** (2010), 149–155. https://doi.org/10.1007/s11589-009-0060-z
17. S. Mojtabazadeh-Hasanlouei, M. Panji, M. Kamalian, Attenuated orthotropic time-domain half-space BEM for SH-wave scattering problems, *Geophys. J. Int.*, **229** (2022), 1881–1913. https://doi.org/10.1093/gji/ggac032
18. C. Song, H. Geng, Y. Wang, U. B. Waheed, C. Liu, Simultaneous P- and S-wave seismic traveltime tomography using physics-informed neural networks, *Geophys. Prospect.*, **73** (2025), e70034. https://doi.org/10.1111/1365-2478.70034
19. K. Shaker, M. Eskandari-Ghadi, S. Mohammadi, Meshless method for wave propagation in poroelastic transversely isotropic half-space with the use of perfectly matched layer, *Int. J. Numer. Anal. Methods Geomech.*, **48** (2024), 3751–3779. https://doi.org/10.1002/nag.3797
20. S. Hou, J. Li, L. Sun, A GFDM with radial PML for SH-wave scattering problems in an orthotropic half plane, *Appl. Math. Lett.*, **171** (2025), 109661. https://doi.org/10.1016/j.aml.2025.109661
21. H. Xue, X. Zhang, J. Cheng, Transient analyses of underwater acoustic propagation with the modified meshfree radial point interpolation method and Newmark time integration techniques, *Ocean Eng.*, **304** (2024), 117842. https://doi.org/10.1016/j.oceaneng.2024.117842
22. C. Z. Shi, H. Zheng, P. H. Wen, Y. C. Hon, The local radial basis function collocation method for elastic wave propagation analysis in 2D composite plate, *Eng. Anal. Boundary Elem.*, **150** (2023), 571–582. https://doi.org/10.1016/j.enganabound.2023.02.021
23. Z. Liu, Z. Wang, L. Guo, D. Wang, F. Wu, A fast-multi-pole accelerated method of fundamental solutions for 2-D broadband scattering of SH waves in an infinite half space, *J. Vibroeng.*, **21** (2019), 250–264. https://doi.org/10.21595/jve.2018.19515

24. C. Yang, Efficient forward and inverse approaches for guided-wave scattering, *Eng. Anal. Boundary Elem.*, **186** (2026), 106680. https://doi.org/10.1016/j.enganabound.2026.106680
25. C. Yang, J. Nakaoka, S. Hirose, Semi-analytical FEM for modelling 3D guided waves scattering in an infinite plate, *Appl. Math. Model.*, **148** (2025), 116236. https://doi.org/10.1016/j.apm.2025.116236
26. C. Yang, R. Qin, S. Hirose, Semi-analytical FEM for modeling 2D guided wave scattering by interface delamination in composite laminates, *Eng. Anal. Boundary Elem.*, **179** (2025), 106427. https://doi.org/10.1016/j.enganabound.2025.106427
27. C. S. Chen, A. Karageorghis, Y. Li, On choosing the location of the sources in the MFS, *Numer. Algors.*, **72** (2016), 107–130. https://doi.org/10.1007/s11075-015-0036-0
28. W. Chen, M. Tanaka, A meshless, integration-free, and boundary-only RBF technique, *Comput. Math. Appl.*, **43** (2002), 379–391. https://doi.org/10.1016/s0898-1221(01)00293-0
29. A. Canelas, B. Sensale, A boundary knot method for harmonic elastic and viscoelastic problems using single-domain approach, *Eng. Anal. Boundary Elem.*, **34** (2010), 845–855. https://doi.org/10.1016/j.enganabound.2010.05.010
30. L. Sun, C. Zhang, Y. Yu, A boundary knot method for 3D time harmonic elastic wave problems, *Appl. Math. Lett.*, **104** (2020), 106210. https://doi.org/10.1016/j.aml.2020.106210
31. M. Lei, T. Li, H. Meng, Comparative analysis of the improved boundary knot and fundamental solutions methods for complex multi-connected Helmholtz-type equations, *Appl. Math. Model.*, **142** (2025) 115971. https://doi.org/10.1016/j.apm.2025.115971
32. F. Wang, Y. Gu, W. Qu, C. Zhang, Localized boundary knot method and its application to large-scale acoustic problems, *Comput. Methods Appl. Mech. Eng.*, **361** (2020), 112729. https://doi.org/10.1016/j.cma.2019.112729
33. X. Yue, F. Wang, P. W. Li, C. M. Fan, Local non-singular knot method for large-scale computation of acoustic problems in complicated geometries, *Comput. Math. Appl.*, **84** (2021), 128–143. https://doi.org/10.1016/j.camwa.2020.12.014
34. Q. Zhang, Z. Ji, L. Sun, An improved localized boundary knot method for 3D acoustic problems, *Appl. Math. Lett.*, **149** (2024), 108900. https://doi.org/10.1016/j.aml.2023.108900
35. F. Wang, C. Wang, Z. Chen, Local knot method for 2D and 3D convection–diffusion–reaction equations in arbitrary domains, *Appl. Math. Lett.*, **105** (2020), 106308. https://doi.org/10.1016/j.aml.2020.106308
36. D. L. Young, K. H. Chen, C. W. Lee, Singular meshless method using double layer potentials for exterior acoustics, *J. Acoust. Soc. Am.*, **119** (2006), 96–107. https://doi.org/10.1121/1.2141130
37. J. Huang, A. Wood, Numerical simulation of electromagnetic scattering induced by an overfilled cavity in the ground plane, *IEEE Antennas Wireless Propag. Lett.*, **4** (2005), 224–228. https://doi.org/10.1109/lawp.2005.851101
38. Z. Tang, Z. Fu, D. Zheng, J. Huang, Singular boundary method to simulate scattering of SH wave by the canyon topography, *Adv. Appl. Math. Mech.*, **10** (2018), 912–924. https://doi.org/10.4208/aamm.oa-2017-0301
39. W. Qu, C. M. Fan, Y. Gu, Localized method of fundamental solutions for interior Helmholtz problems with high wave number, *Eng. Anal. Boundary Elem.*, **107** (2019), 25–32. https://doi.org/10.1016/j.enganabound.2019.06.018
40. L. Sun, Z. Ji, Q. Zhang, X. Wei, A localized meshless collocation method based on fundamental solutions for 3D uncoupled transient thermoelastic problems, *Int. J. Heat Mass Transfer*, **232** (2024), 125945. https://doi.org/10.1016/j.ijheatmasstransfer.2024.125945

41. Ö Oruç, A local meshfree radial point interpolation method for Berger equation arising in modelling of thin plates, *Appl. Math. Model.*, **122** (2023), 555–571. https://doi.org/10.1016/j.apm.2023.03.014
42. L. Chen, R. Huo, H. Lian, B. Yu, M. Zhang, S. Natarajan, et al., Uncertainty quantification of 3D acoustic shape sensitivities with generalized nth-order perturbation boundary element methods, *Comput. Methods Appl. Mech. Eng.*, **433** (2025), 117464. https://doi.org/10.1016/j.cma.2024.117464
43. H. Jin, X. Wei, L. Sun, Z. Fu, Dynamic analysis of 3D saturated poroelastic media with singular boundary method, *Comput. Math. Appl.*, **217** (2026), 115–137. https://doi.org/10.1016/j.camwa.2026.05.024